

# Stem-cell differentiation underpins reproducible morphogenesis

Dominic K Devlin<sup>1\*</sup>, Austen RD Ganley<sup>1,2</sup>, and Nobuto Takeuchi<sup>1,3,4</sup>

<sup>1</sup>School of Biological Sciences, University of Auckland, Private Bag 92019, Auckland 1142, New Zealand

<sup>2</sup>Digital Life Institute, University of Auckland, Private Bag 92019, Auckland 1142, New Zealand

<sup>3</sup>Research Centre for Complex Systems Biology, Universal Biology Institute, University of Tokyo, Komaba 3-8-1, Meguro-ku, Tokyo 153-8902, Japan

<sup>4</sup>Department of Biology, Faculty of Sciences, Kyushu University, Fukuoka, Japan  
\*ddev825@aucklanduni.ac.nz

March 26, 2025

## Summary

Morphogenesis of complex body shapes is reproducible despite the noise inherent in the underlying morphogenetic processes. However, how these morphogenetic processes work together to achieve this reproducibility remains unclear. Here, we ask how morphogenetic reproducibility is realised by developing a computational model that evolves complex morphologies. We find that evolved, complex morphologies are reproducible in a sizeable fraction of simulations, despite no direct selection for reproducibility. Strikingly, reproducible morphologies had also evolved stem-cell systems. We show that reproducibility is caused by a morphogenetic division of labour based on these stem-cell systems, where moving, dividing stem cells “shape” morphologies and irreversibly differentiate into stationary, non-dividing cells. These results suggest that stem-cell systems observed in natural development play fundamental roles in morphogenesis in addition to their known role of producing specialised cell types. This previously-unrecognised role of stem-cell systems has major implications for our understanding of how morphologies are generated and regenerated.

## 1 Introduction

Morphogenesis is the multifaceted process that transforms a relatively homogeneous starting material — a fertilised zygote — into the complex morphological structures, such as organs, tissues and appendages, that constitute a mature organism [1, 2]. This transformation occurs through a combination of chemical-level pattern formation and cellular-level shape formation [3, 4]. At the chemical level, reacting and diffusing chemicals produce spatial patterns, such as stripes and segments [5, 6]. At the cellular level, processes such as cell motion, division, contraction and differential adhesion interact with chemical-level pattern formation to produce morphological shapes, such as tails, tubes, branches and limbs [1, 2, 7, 8, 9]. For extant animals, the morphological structures produced by these processes are not only complex, but also reproduced with astonishing precision across generations. Understanding how complex morphogenesis is made reproducible has intrigued the minds of thinkers since Pythagoras and

Aristotle [10], and is a focal point of developmental biology [4, 11, 12, 13].

Reproducibility of complex morphologies requires both cell-level and chemical-level processes to be robust to noise [14, 15]. Much attention has been devoted to understanding the robustness of chemical-level pattern formation to molecular sources of noise, such as fluctuations in chemical concentrations [16], resulting in the characterisation of chemical-level processes that enhance pattern reproducibility, such as genetic feedback loops and signal transduction pathways [17, 18, 19, 20, 21, 22, 23, 24]. In contrast, much less is known about the cellular processes underlying the robustness of morphogenesis to cell-level sources of noise, such as stochasticity in the motion and geometry of cells [25]. To address this issue, previous studies have taken a targeted approach in which they selected a set of cell-level processes, such as cell-cell signalling and differential adhesion, and examined each process to determine whether it increases morphogenetic reproducibility [26, 27].

Here, we instead asked whether morphogenetic reproducibility is an emergent by-product of complex morphogenesis that evolves even if reproducibility is not explicitly selected for, and, if so, how this reproducibility is realised—a non-prescriptive approach pioneered by Hogeweg [28, 29, 30]. To answer these questions, we computationally generated an ensemble of “morphogeneses” by repeatedly evolving a population of organisms selected for complex, multicellular shapes. We found that a sizeable fraction of evolved organisms had high reproducibility, even though reproducibility was not explicitly selected. Strikingly, these organisms shared one cell-level feature responsible for morphogenetic reproducibility: a “morphogenetic division of labour”, where moving and dividing stem cells “shape” morphologies, and non-moving and non-dividing differentiated cells spatially “anchor” this shaping process, thereby enhancing morphogenetic reproducibility.

## 2 Results

### 2.1 Multi-scale model

We set out to investigate whether complex, evolvable morphogenesis is intrinsically reproducible by developing a computational model consisting of cells equipped with only the basic properties necessary for morphogenesis that are not species-specific: cell motion, gene regulation, cell-cell signalling, differential adhesion, and unpolarised cell contractions. Although limiting the model to these basic properties constrains the types of morphologies we can evolve, it increases the likelihood that the morphologies we do evolve could be realised across a broad range of developmental contexts in nature.

To capture the noisy dynamics of natural-world morphogenesis, we employed the Cellular Potts Model (CPM), which uses a Metropolis algorithm to simulate stochastic cell motion and cell geometry dynamics (Methods 4.1) [31, 32]. The CPM models the development of a single organism on a two-dimensional square grid ( $250 \times 250$  pixels) starting from a single cell. A collection of neighbouring pixels on the grid represents a cell (Fig 1A). Pixels not occupied by cells represent the medium (Fig 1A), which is akin to an extracellular matrix or fluid [33]. Cell motion occurs through stochastic extensions and retractions of cell boundaries, mimicking natural cell motion [34]. These extensions and retractions are generated by pixel copying at the cell boundaries (Fig 1A; Methods 4.1). The probability that a pixel copy occurs is determined by free energy contributions from cell-cell adhesion, cell-medium adhesion, cell shape, and cell size, as described later. Pixels on the grid are chosen in a random order with replacement for copy attempts. The unit of time is the number of pixel copy attempts equal to the total number of pixels on the grid, hereon referred to as a developmental time step (DTS).

To simulate the development of an organism, the CPM is run for 12,000 DTS, which is approximately the minimum time it takes for a fast-growing organism to reach the edge of the

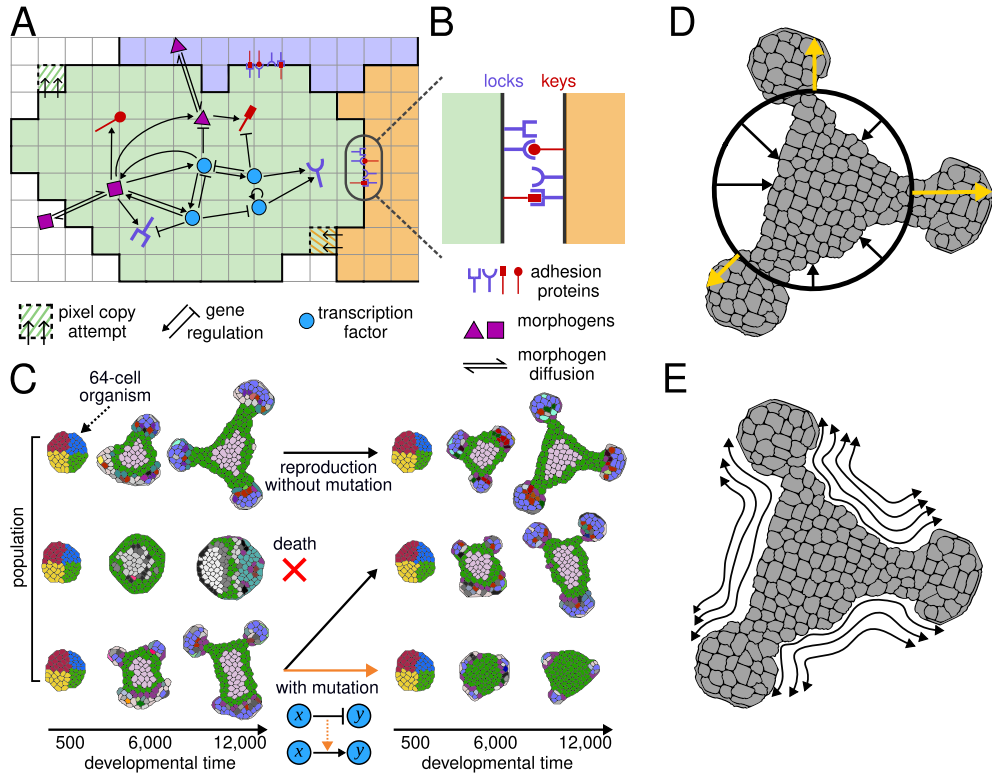


**Figure 1: Multi-scale model of morphogenesis evolution.** **A** Three neighboring cells on a CPM grid. A cell consists of one or more pixels. Each cell is colored by its “cell state” defined by the concentrations of all its proteins converted to boolean values (the medium is represented by white pixels). Pixels with alternating stripes indicate pixel copies at cell boundaries. Each cell contains a genome that encodes transcription factors (TFs; circles, squares, triangles), adhesion proteins (sticks with a lock or key) and contractile proteins (not shown). Arrows indicate regulation of gene expression by TFs (arrow head for activation, blunt head for inhibition). Double harpoon arrows indicate diffusion of morphogens (membrane-permeable TFs). **B** Adhesion proteins facilitate the binding of cells to each other via a lock and key mechanism, or to the surrounding medium (not shown). **C** A population consists of 60 organisms (only three depicted). Organisms undergo a developmental phase on separate CPM grids for 12,000 DTS, and then a reproduction phase, where organisms with complex morphologies are selected. Reproduction can occur without mutation (black arrows) or with mutation (orange arrow), with mutation determined probabilistically. Mutations change the topology of the GRN (dashed orange arrow), with the example showing a change from inhibition of gene  $y$  by gene  $x$  to activation of gene  $y$  by gene  $x$ . **DE** Illustration of the two measurements used to select for morphological complexity (described in Methods 4.5). The cells are all coloured grey to emphasise that only the shape, not cell states, determine the complexity score. (D) depicts the measurement for deviation of the morphology from a perfect circle; black arrows mark areas where the organism’s radius (measured from its centre of mass) is smaller than that of a circle, while yellow arrows indicate regions where the radius is larger. (E) depicts regions of inward folding using double sided arrows, with the number and length of arrows indicated the extent of inward folding.

grid. Each organism starts as a “zygote” that rapidly divides six times to create a ball of 64 cells of approximately 75 pixels each (Fig. 1C, Methods 4.2). This rapid cell division without growth mimics the earliest cell divisions that occur in animal embryos after fertilisation [2]. After the 64-cell stage, cells grow and divide if they are mechanically stretched, mimicking the mechanical induction of cell growth and division observed in natural development [35, 36, 37]. The size of each cell, measured in pixels, is energetically constrained to a target size: the more a cell’s size departs from the target size, the larger the free energy. The target size is initially set to each cell’s actual size following the six rapid divisions. When a cell is stretched to three pixels above its target size, its target size is increased to its current size (Methods 4.2). Cell stretching is induced by adhesion to neighbouring cells and the extracellular medium, although it can also occur stochastically. When a cell reaches a size of 100 pixels, it divides by splitting along its minor axis into two daughter cells of approximately equal size. Protein concentrations remain the same for both daughter cells upon cell division and the target sizes of the daughter

cells are decreased to their current sizes.

To model the dependency of morphogenesis on spatial patterns of protein concentrations, we coupled the CPM dynamics to gene expression dynamics, as previously done [29, 30, 38, 39, 40, 41]. Specifically, we equip each organism with a set of protein-encoding genes, such as transcription factors (TFs), that form an gene regulatory network (GRN). A GRN is a graph consisting of nodes representing proteins and edges representing TF-mediated activation or inhibition of gene expression (Fig 1A). Concentrations of proteins within a cell are determined by numerically integrating a set of ordinary differentiation equations given by the GRN (Methods 4.3). To model cell-cell signalling, three TFs (hereafter called morphogens) diffuse between cells and into the medium (Fig 1A; Methods 4.3). These morphogens model morphogens encountered in real biological development, such as Wnts and BMPs [19, 42, 43], and they allow different cells to express different proteins even though all cells within an organism have an identical GRN. The diffusivity is the same for all three morphogens (methods 4.3).

The other way differential protein expression between cells can occur in real biological embryos is by the asymmetric distribution of “maternal factors” at the zygote stage [44]. To model this, two non-morphogen TFs are defined as maternal factors. One maternal factor is restricted to the left of the zygote’s vertical centre line; the other, to the bottom side of the zygote’s horizontal centre line. The first two of the six rapid cell divisions occur along these centre lines, so that each cell at the four-cell stage has a unique combination of maternal factor concentrations (illustrated in Fig. 1C).

Organisms carry two other types of genes: those encoding adhesion proteins and contractile proteins (Methods 4.4). Adhesion proteins modulate the adhesiveness of cells to neighbouring cells and the extracellular medium (Fig. 1AB). These proteins model cell-surface proteins, such as cadherins and integrins, which are essential drivers of cell behaviours necessary for morphogenesis, such as cell migration and sorting [2, 45]. Adhesion proteins that determine the strength of cell-cell adhesion are either locks or keys, where the adhesion strength between two neighbouring cells scales with the number of compatible lock-key pairs that the two cells express. Similarly, adhesion of a cell to the medium scales with the number of medium-adhesion proteins expressed by the cell (Methods 4.4). Contractile proteins make the cell less deformable by energetically constraining the cell to an elliptic shape, where the length of the major axis of the elliptic shape scales with the number of expressed contractile proteins (Methods 4.4). These proteins model unpolarised contractions of the cell cortex, mirroring those observed in biological cells by the accumulation of actin filament stress [46].

We distinguish cells based on the proteins they express by assigning each cell a cell state defined as a vector of boolean values, where each boolean value indicates whether a contractile or adhesion protein is expressed or not expressed (Methods 4.6). All cells with the same state are shown with the same colour on the CPM grid (Fig. 1). Cell states are only used to visualise and analyse model outcomes and do not play any role in model dynamics.

To simulate the evolution of morphogenesis, we established an initial population of 60 organisms (Fig. 1C; Methods 4.5), with each assigned a different randomly generated GRN. Each organism develops on a separate CPM grid. We applied a genetic algorithm to select for morphological complexity by measuring inward folding and deviation of the morphological shape from a circle at the end of the 12,000 DTS (Fig. 1DE; Methods 4.5). The 15 organisms with the highest morphological complexity reproduce four times to populate the next generation, and their GRNs undergo a single mutation with a probability of 50%. A mutation changes the regulatory effect of one TF on one gene, such as causing a TF to switch from inhibiting the expression of a gene to activating its expression (see Fig. 1C). The GRNs used in our main set of simulations, described subsequently are composed of nine transcription factors (including the three morphogens), 15 adhesion proteins and two contractile proteins. However, we also run simulations with GRNs composed of different numbers of genes to confirm subsequent results (Fig. S7EFGH)

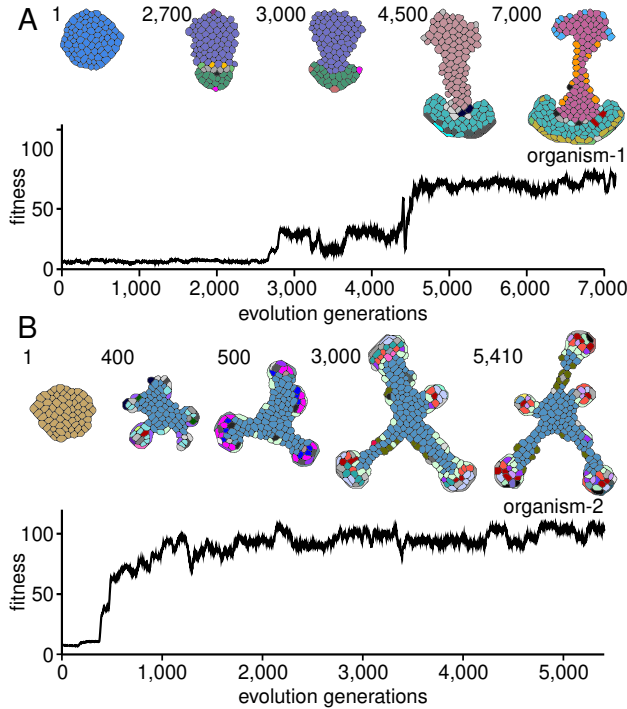


Figure 2: **Computational simulations showing the evolution of complex morphologies.** **AB** The plots show a five-generation moving average of population fitness (morphological complexity) over evolution. The organism morphologies above the plots each depict a separate organism at the end of its development (12,000 DTS) from six different generations over the course of evolution. The generation number of each organism morphology is shown to its left. “Evolved organisms”, defined as the most morphologically complex organism from the final generation of the simulation, are shown on the far right. The evolved organisms in (A) and (B) are hereafter referred to as organism-1 and organism-2, respectively.

## 2.2 Reproducibility is not an intrinsic property of complex morphogenesis

To investigate whether complex morphogenesis is intrinsically reproducible, we conducted 126 independent evolutionary simulations of our model. We ran these for at least  $2.5 \times 10^3$  generations, which is usually sufficient to reach a plateau in fitness (Fig. S1). We then identified the fittest (i.e., most morphologically complex) organism from the final generation (hereafter referred to as an “evolved organism”) from each simulation. To ensure that we were analysing the reproducibility of complex morphologies, we removed 36 evolved organisms that did not reach an arbitrary threshold of complexity (our results are similar when a different threshold is used; Fig. S2A). The 90 organisms above this threshold each display a different morphology (Fig. S1), with the evolution of two representative organisms illustrated in Fig. 2AB.

We examined whether the 90 evolved organisms with complex morphologies display reproducible morphogenesis by repeatedly simulating their development (60 replicates per organism, hereafter referred to as developmental replicates). To quantify reproducibility, we measured a “reproducibility score”, which indicates how geometrically similar the morphologies of replicates are to each other (Methods 4.7). The reproducibility score depends on the geometry, size and time taken to generate the morphology but is invariant to reflection, rotation and translation of the morphology. Figure 3A and B illustrate two developmental replicates of an organism with high reproducibility and an organism with low reproducibility, respectively (hereafter referred to as organism-1 and organism-2). The distribution of reproducibility scores across all 90 evolved organisms is bimodal (bimodality coefficient = 0.69, Fig. 3C), with 19 organisms in the upper mode, which we term highly reproducible (including organism-1; Fig. 3D shows four other examples), 65 organisms in the lower mode, which we term poorly reproducible (including organism-2; Fig. 3E shows four other examples), and six that are between the two modes,

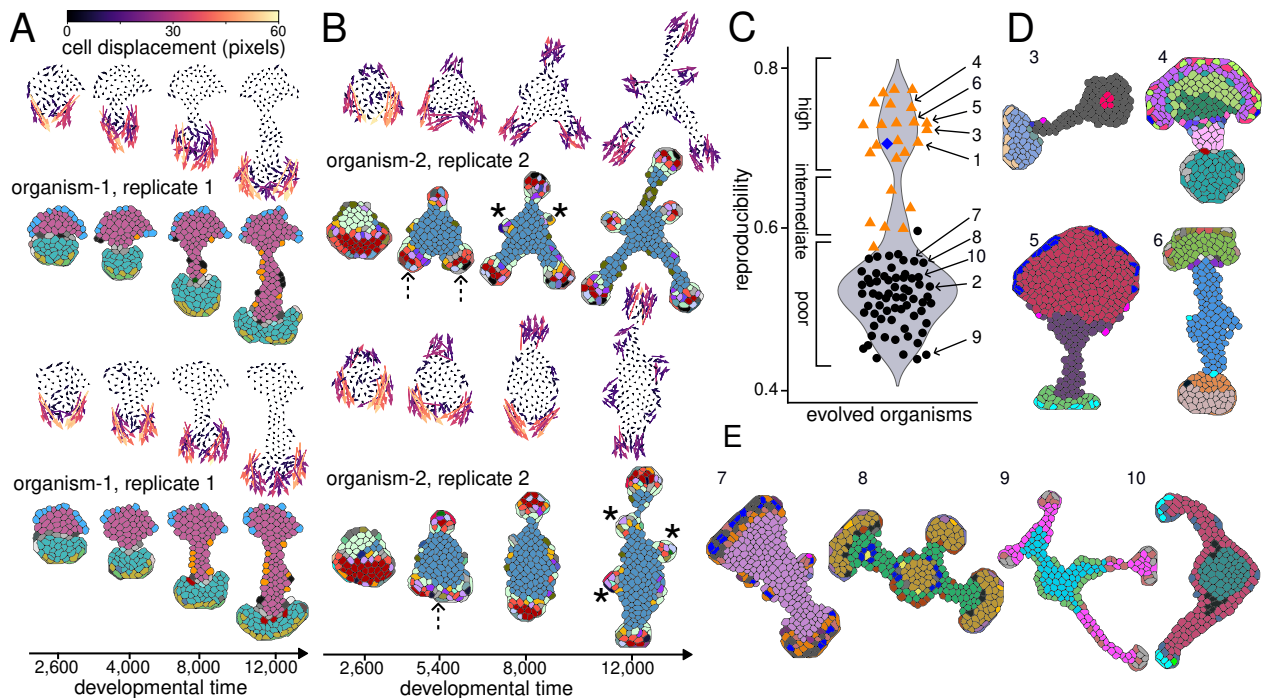


Figure 3: **Both highly and poorly reproducible organisms evolve in response to selection for complex morphologies.** **AB** Two developmental replicates of organism-1 (A) and organism-2 (B) are depicted after 400, 2,600, 4,000, 8,000 and 12,000 DTS, showing a difference in their reproducibility. Dashed arrows in (B) indicate the presence (replicate-1) or absence (replicate-2) of a bifurcation in collective cell motion; asterisks indicate protrusions. Vector plots above the organisms show the displacement of the centre of mass of each cell during 2,000 DTS at each respective time point, with colours indicating magnitude (the lighter, the larger). **C** Reproducibility scores for the 90 organisms that evolved a complex morphology. Circles indicate organisms with a single strongly connected component (SCC, defined in Section 2.5) (mean reproducibility= 52.0%,  $n = 65$ ); filled triangles indicate organisms with multiple SCCs with unidirectional transitions between them (mean reproducibility= 72.1%,  $n = 24$ ). The blue diamond is an organism with multiple SCCs without unidirectional transitions (Fig. S3D). Numbered arrows refer to the organisms in panels A, B, D, and E. The data is overlaid on a violin plot that illustrates the bimodality in reproducibility scores. **D** Four organisms with highly reproducible morphologies. **E** Four organisms with poorly reproducible morphologies.

which we term intermediately reproducible (see Fig. S3EF for information about intermediately reproducible organisms). The bimodal distribution implies that evolved organisms consist of a mixture of two populations, suggesting that variation in reproducibility is a consequence of the two groups having different properties.

The observed variation in morphological reproducibility might trivially arise from variation in morphological complexity because morphogenesis can become more sensitive to noise as the resulting morphology becomes more complex [26, 28]. To test this possibility, we compared the morphological complexity scores of evolved organisms. The result shows that highly reproducible organisms had 24% lower morphological complexity on average than poorly reproducible organisms (Fig. S2). To determine whether this difference in complexity scores was indeed responsible for differences in morphological reproducibility, we conducted a regression analysis of evolved organisms' morphological reproducibility against their complexity scores (Text S1, which also includes an alternative test independent of our complexity and reproducibility measures). The result shows that, when matched for morphological complexity, the difference in reproducibility of organisms categorised as highly and poorly reproducible remains significant, although there is some correlation between complexity and reproducibility (Fig. S2E). These results indicate that variation in morphological reproducibility cannot be exclusively explained by variation in morphological complexity, suggesting the presence of reproducibility-conferring properties in a subset of the evolved organisms.

## 2.3 Highly and poorly reproducible organisms have distinct cell-state transition dynamics

We wondered if the property conferring high reproducibility onto organisms is related to cell motion, given that cell motion is a driver of morphogenesis. To investigate this, we visualised the velocity of every cell at multiple time points during development of evolved organisms. We found that in organism-1, which is highly reproducible, cells at the bottom of the organism collectively move consistently downwards and radiate slightly outwards, like a travelling wave (Fig. 3A; Video S1), while cells at the top of the organism show little motion. These position-dependent collective cell motions generate a “cap” of moving cells and a “stalk” of stationary cells forming in the wake of the moving cap (Fig. 3A). Cap and stalk cells are in distinct cell states as indicated by the colours in Fig 3A. Importantly, these collective cell motions are consistent across developmental replicates (Fig. 3A). By contrast, in organism-2, which is poorly reproducible, patterns of collective cell motion are inconsistent across developmental replicates (Fig. 3B; Video S2). These inconsistencies arise in two related ways, which we call “bifurcations” and “protrusions.” Bifurcations are the spontaneous splitting of a group of moving cells into two separate groups caused by some of the moving cells transitioning into stationary cells at the bifurcation point (Fig. S3AB). Bifurcations occur inconsistently across developmental replicates of organism-2 (dashed arrows, Fig. 3B). Protrusions are the spontaneous onset of collective cell motion caused by stationary cells transitioning into moving cells (Fig. S3AC). For instance, in replicate 1 of organism-2, two groups of initially stationary cells protrude to form bulges around 8,000 DTS (Fig 3B, top), whereas in replicate 2 this occurred in three groups of cells at locations different from replicate 1 around 12,000 DTS (Fig 3B, bottom). Both bifurcations and protrusions are caused by transitions between moving and stationary cells, suggesting that poorly reproducible organisms may be more prone to stochastic transitions in cell motion.

Transitions between moving and stationary cells appear to occur via cell-state transitions (Fig. 3AB; Fig. S4BF). Therefore, we next tested whether highly and poorly reproducible organisms have different cell-state transition dynamics. To this end, we recorded all cell-state transitions of all cells in each evolved organism to generate the “cell state space” of that organism, which is defined as the graph consisting of nodes representing cell states and edges representing all possible transitions between cell states (see Methods 4.6 for details). Since each cell state space contains numerous nodes and edges, we simplified the state spaces in two steps. First, we pruned infrequently observed cell states and cell-state transitions (Methods 4.6). Second, we split the cell state space into strongly connected components (SCCs), where an SCC is defined as a set of cell states for which a pathway of transitions exists from any cell state to any other cell state within that set. We found that almost all (64 out of 65) poorly reproducible organisms had just a single SCC, as illustrated for organism-2 in Fig. 4B. In contrast, all 19 highly reproducible organisms and most (five out of six) intermediately reproducible organisms had cell state spaces containing multiple SCCs, as illustrated for organism-1 in Fig. 4A. Moreover, most (24 out of the 25) organisms with multiple SCCs had at least one SCC that unidirectionally transitioned to another SCC, as illustrated in Fig. 4A (see Fig. S3D for details about the one organism without unidirectional SCC transitions). The difference in reproducibility between organisms with a single SCC and those with multiple SCCs is statistically significant ( $p < 10^{-12}$ , two-tailed t-test), suggesting that the presence of multiple SCCs is involved in morphogenetic reproducibility.

We next sought to determine whether the difference in the number of SCCs can explain why highly reproducible organisms have less stochastic (i.e., more consistent) transitions between stationary and moving cell states than poorly reproducible organisms. In organisms with one SCC, the single SCC includes both stationary and moving cell states. Thus, transitions in cell motion are reversible since a transition pathway exists between any two cell states within the same SCC (i.e., all cell-state transitions can be reversed). By contrast, in organisms with mul-

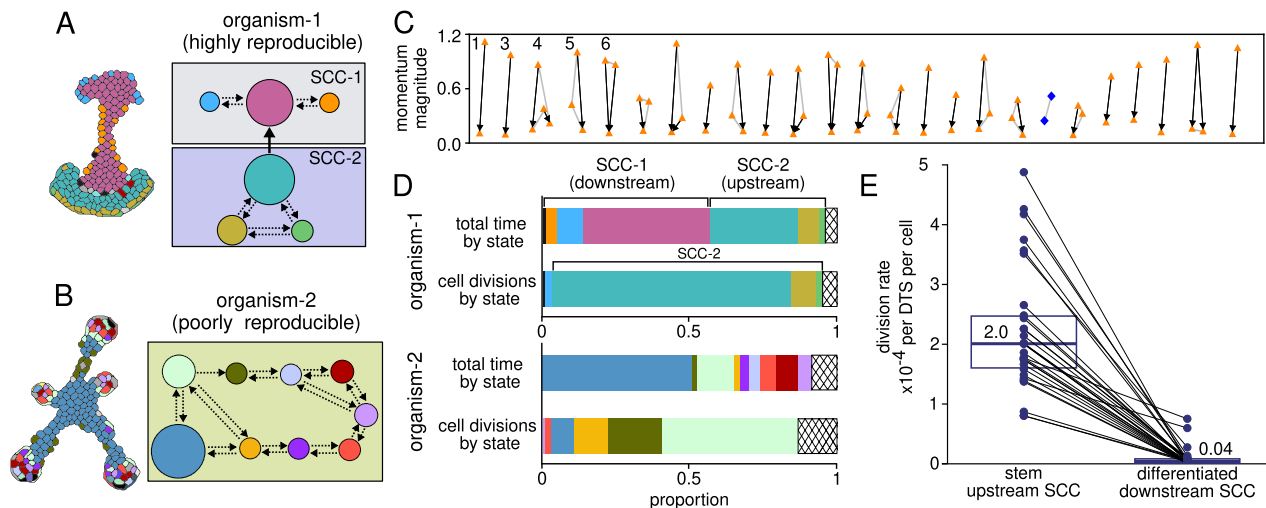


Figure 4: **Highly reproducible organisms have moving and dividing cells that undergo unidirectional transitions to non-moving and non-dividing cells.** **AB** Simplified cell state spaces, consisting of cell states (nodes) and cell-state transitions (arrows) after partitioning into strongly connected components (SCCs, coloured boxes) for (A) organism-1, which is highly reproducible, and (B) organism-2, which is poorly reproducible. Node sizes depict cell state frequency over all of development; node colours correspond to cell states from organism-1 and organism-2, respectively (shown to the left of each state space). See Fig. S4IJ for the state spaces without pruning of nodes and edges. **C** Average cell momentum magnitude for each SCC from the 25 organisms with multiple SCCs. Momentum is the distance travelled of a cell per DTS multiplied by its size in pixels (see Methods 4.8). Black arrows indicate unidirectional transitions between SCCs. Grey lines connect SCCs from the same organism that do not have unidirectional SCC transitions between each other. Filled orange triangles are SCCs from organisms that have unidirectional SCC transitions. All transitory SCCs are excluded (see Methods 4.6 for information about transitory SCCs). Blue diamonds are SCCs from the highly reproducible organism that does not have unidirectional SCC transitions. The first five numbered organisms correspond to those from Fig. 3D. **D** Stacked bar charts showing the proportion of developmental time spent in each cell state and the proportion of cell divisions undergone by each state across all cells during developmental replicate-1 of organism-1 from Fig 3A and development replicate-1 of organism-2 from Fig 3B. Diagonal lattices are pruned states. **E** The rate at which cells divide per developmental time when their state belongs to an upstream SCC (left) or a downstream SCC (right). Each data point represents an SCC from (C). Black lines connect upstream SCCs to their counterpart downstream SCCs. Boxes show medians and interquartile ranges (IQR); the downstream SCC box is tiny because most division rates are either very low or 0. Numbers on top of the box plots are median cell division rates.

multiple SCCs, it is possible that stationary and moving cell states are partitioned into separate SCCs to limit cell-motion transitions. To test if this partitioning has evolved, we determined whether different SCCs have different cell-motion properties in organisms with multiple SCCs by measuring the momentum of cells in each SCC (Methods 4.8). The result shows a significant disparity (mean 6.7-fold difference) in the average magnitude of cell momentum between SCCs across all highly reproducible organisms (Fig. 4C), indicating that moving and stationary states are indeed partitioned into separate SCCs. Strikingly, the transitions are always from high momentum SCCs to low momentum SCCs (black arrows in Fig. 4C)). Thus, cells in upstream SCCs are motile, whereas those in downstream SCCs are stationary. This suggests that organisms with multiple SCCs establish a “morphogenetic division of labour”, whereby moving cells (in upstream SCCs) “shape” morphologies and unidirectionally transition into stationary cells (in downstream SCCs) that “maintain” the morphologies shaped by moving cells. Restricting cell-motion transitions to unidirectional SCC transitions increases reproducibility by preventing protrusions, which require transitions from stationary to moving cells.



## 2.4 Multiple SCCs in reproducible organisms resemble stem-cell systems

Our results suggest that having a morphogenetic division of labour between SCCs is important for reproducibility. Intriguingly, these morphogenetic divisions of labour resemble stem-cell systems, as upstream SCCs (corresponding to stem or progenitor cells) unidirectionally transition to downstream SCCs (corresponding to differentiated cells). This unidirectional transitioning is equivalent to irreversible differentiation — a hallmark of stem-cell systems. Another hallmark of stem-cell systems is that stem or progenitor cells undergo more rapid cell division than differentiated cells [47, 48]. To examine whether this other hallmark is also displayed by our organisms with a morphogenetic division of labour, we compared how often cells in upstream versus downstream SCCs divide (Fig. 4DE). We found that cells in upstream SCCs divide a median of 49.6 times more frequently than those in downstream SCCs. Thus, the morphogenetic division of labour encompasses not only differential cell motion, but also differential cell divisions between SCCs. Hereafter, we refer to upstream SCCs and downstream SCCs as stem-cell types and differentiated-cell types, respectively. We define a stem-cell system as comprising one stem-cell type and its counterpart differentiated-cell types (some organisms have multiple stem-cell types, thus multiple stem-cell systems).

## 2.5 Stem-cell systems elevate morphogenetic reproducibility by regulating cell-motion transitions at cell-type boundaries

For morphogenetic division of labour to elevate reproducibility, differentiation of stem cells (which shape morphology by moving and dividing) to differentiated cells (which maintain morphology by neither moving nor dividing) must be consistent during development and across developmental replicates. Thus, we next asked how this consistency is achieved. We noticed that the spatial layout of stem and differentiated cells tends to mirror the topology of the cell state space in organisms with stem-cell systems. Specifically, cells in states belonging to the same SCC are spatially clustered within an organism such that each cluster corresponds to a distinct stem or differentiated cell type (Figs. 5A and S4K). For example, in organism-6, there are two clusters of cells at the top and bottom of the organism, each corresponding to a separate stem-cell type, denoted as type-1 and type-2 (Fig. 5A). These stem-cell clusters are present from the start of organism-6 development (i.e., the 64-cell stage) because of the initial heterogeneous distribution of maternal factors. After the 64-cell stage, stem cells initially differentiate exclusively at the boundary between the type-1 and type-2 stem cells and, subsequently, exclusively at the boundary between stem cells and differentiated cells (Video S3). This boundary-localised differentiation results in a cluster of differentiated cells consistently forming between the stem-cell clusters (Fig. 5A).

Boundary-localised differentiation suggests that stem-cell differentiation is spatially regulated. To determine how this regulation is achieved, we first focused on organism-6 as it has two separate examples of stem-cell differentiation due to it having two stem-cell types. We hypothesised that boundary-localised differentiation is caused by morphogen-mediated interactions between stem and differentiated cells as morphogens provide a means to spatially regulate gene expression. To test this, we made a contour plot of morphogen concentrations in organism-6 (Fig. 5B). The plot shows that the concentrations of different morphogens abruptly change at the boundaries between stem and differentiated cells (dashed lines in Fig. 5B). To determine whether gene expression responds to these changes in morphogen concentrations, we plotted the sum of protein concentrations (excluding morphogens) for cells along a cross-section of organism-6 (Fig. 5C). The plot shows that this sum changes abruptly wherever morphogen concentrations abruptly change, suggesting that morphogens regulate gene expression. These results suggest that a specific morphogen profile induces differentiation, with differentiated cells producing this profile and thus localising differentiation to the boundary between stem and dif-

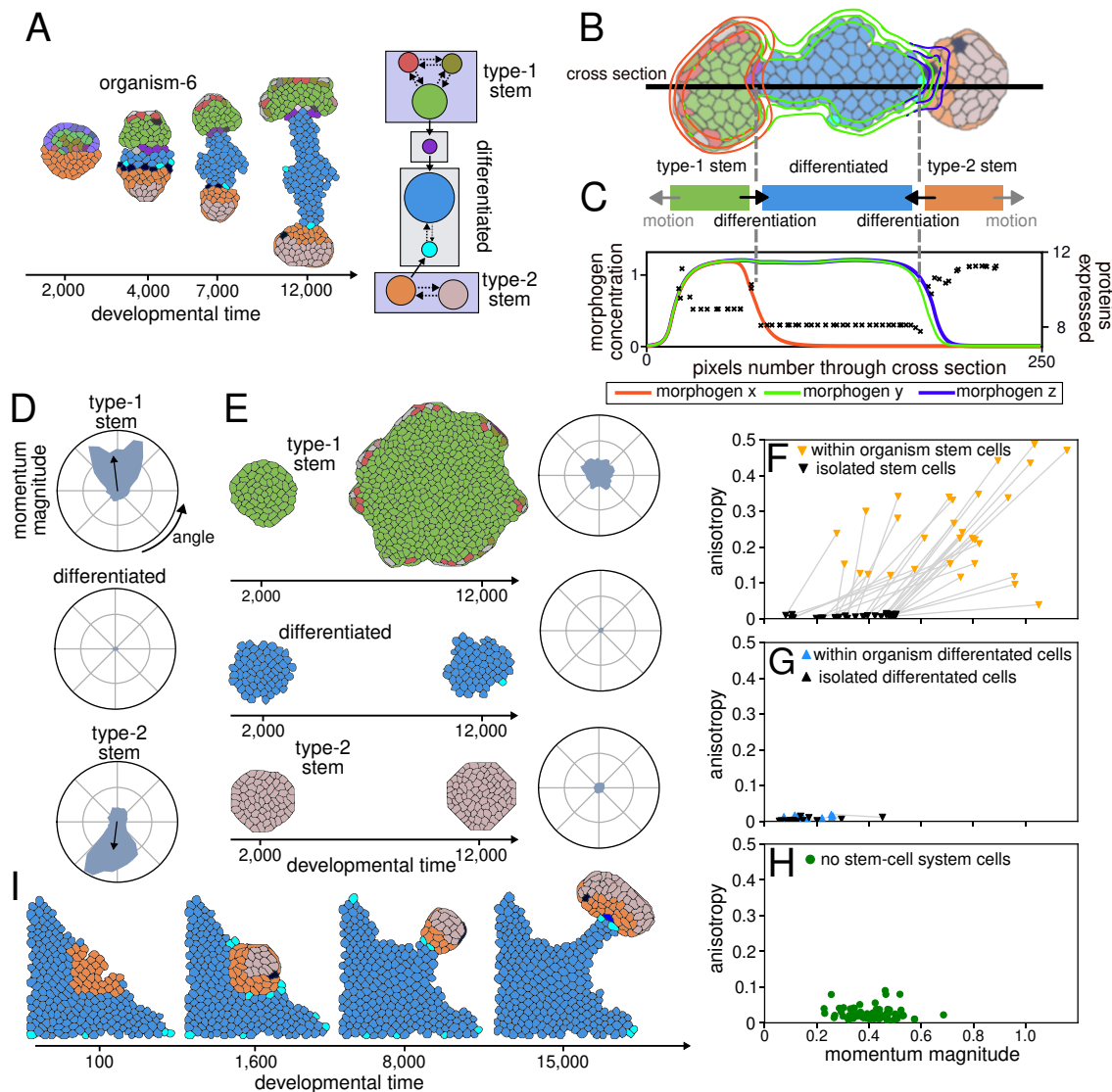


**Figure 5: Mechanisms underlying the consistency of stem-cell differentiation and motion.** **A** The spatial structure of cell types in organism-6 reflects the topology of the cell state space. There are two stem-cell types, one differentiated-cell type, and a transitory SCC (see Methods 4.6 for information about transitory SCCs). The morphology is shown after 2,000, 6,000 and 12,000 DTS. **B** Contours showing the concentrations of the three morphogens ( $x$ ,  $y$  and  $z$ ) overlaid on organism-6 after 9,000 DTS. Each contour joins points of equal concentration of the same morphogen. **C** Schematic depicting type-1, type-2 and differentiated cell clusters from (B), with stem cell motion (grey arrows) and differentiation (black arrows) indicated. Vertical dashed lines indicate cell-type boundaries. Below, morphogen concentrations along the cross-section line are plotted, along with the sums of cell protein concentrations for cells along the cross-section (each cross is one cell). **D** Polar plots of momentum magnitude by angle of motion for each cell type summed over all cells over the 12,000 DTS of organism-6 development (Methods 4.8). **E** Development of type-1, type-2 and differentiated cells in isolation. Polar plots show distributions of cell momentum as in (D). **F** Motion anisotropy of stem cells within organisms (orange) and isolated (black) plotted against average cell momentum magnitude ( $n = 30$  cell types). Grey lines connect a stem cell type within an organism to that stem cell type in isolation. **G** The same as (F), but for differentiated cells ( $n = 26$  cell types). **H** The same as (F), but for cells from organisms with only one SCC ( $n = 65$ ). **I** Developmental trajectory for an arbitrary configuration of type-1 stem and differentiated cells from organism-6 for 15,000 DTS. The initial state of all cells was set to the differentiated blue state from (A), except for a subset of cells on the surface of the triangle that were set to the orange type-2 state from (A).

differentiated cells. To directly test this, we isolated each stem-cell type from the other two cell types, thereby removing the effect of differentiated cells on morphogen profiles. To achieve this isolation, we created organisms in which all cells at the 64-cell stage were set to the state that is most frequently observed for each of the stem-cell types (e.g., the green cell state shown in Fig. 5A for type-1 stem cells). We developed these organisms for 12,000 DTS to test whether isolated type-1 and type-2 stem cells differentiate. We found that neither stem-cell type differentiates (Fig. 5E). These results support the hypothesis that differentiated cells induce stem-cell differentiation, thus localising this differentiation to the boundaries between cell types.

We next asked whether the above findings — that differentiated cells induce stem-cell differentiation — are generalisable to all organisms with stem-cell systems. To answer this, we isolated each of the 30 stem-cell types from the 24 organisms with stem-cell systems from all other cell types and tested whether the isolated stem cells differentiate through the same method as described in the previous paragraph. We found that the great majority (26 out of 30) do not differentiate when isolated from other cell types (Fig. S5 shows why the four exceptions do not counter our hypothesis). This result, along with the observation that every stem-cell type always differentiates at the boundary shared with differentiated cells (Figs. 3A, 5A and S4K), indicates that differentiated cells induce stem-cell differentiation.

The spatial consistency of stem-cell differentiation is crucial but not sufficient for morphogenetic reproducibility. The other critical factor is the motion of stem cells in a consistent direction (e.g., organism-1 Fig. 3A and organism-6 Fig. 5A), as this motion helps to confer consistent shape formation across developmental replicates. Given that stem-cell differentiation is induced by differentiated cells, we hypothesised that the directionality of stem-cell motion is also induced by differentiated cells.

To test this, we determined how stem cells' motion depends on the presence or absence of differentiated cells by measuring the magnitude of stem cells' momentum as a function of the angle of momentum, either in normal development (differentiated cells present) or when each stem cell type is isolated (differentiated cells absent). The result shows that momentum is strongly directional (i.e., anisotropic) when a stem-cell type is in normal development, whereas it is radially symmetrically distributed (i.e., isotropic) when a stem-cell type is isolated (Fig. 5DE shows results for organism-6; see Fig. S5 for other organisms). We quantified this difference in anisotropy by calculating the ratio of the variance in momentum magnitude across angle to the mean momentum magnitude across angle (Methods 4.8). We found that anisotropy of stem-cell motion decreased an average of 65-fold across the 30 stem cell types when stem cells were isolated (Fig. 5F). These results support the hypothesis that the presence of differentiated cells induces directional stem-cell motion.

We next asked how, mechanistically, the presence of differentiated cells induces directional stem-cell motion. We hypothesised that differential expression of adhesion proteins between stem and differentiated cells might drive this motion, as the adhesion energies determined by these proteins are a determinant of cell motion in our model. To test this, we measured the adhesion energy arising from stem-to-stem cell contact, stem-to-differentiated cell contact and differentiated-to-differentiated cell contact across all 30 stem-cell systems (Fig. S6AB). We found that stem-to-stem adhesion energies were lower than stem-to-differentiated adhesion energies in all 30 stem-cell systems (means of 4.1 and 8.1, respectively; Fig. S6AB; differentiated-to-differentiated adhesion energy is variable, with a mean of 10.6). The low stem-to-stem adhesion energies relative to stem-to-differentiated adhesion energies implies that stem cells preferentially adhere to each other rather than to differentiated cells, indicating that clusters of stem cells should move away from areas where they border differentiated cells (this effect is akin to a dewetting of fluid-like tissue from solid-like tissue, a phenomenon observed in both epithelial and mesenchymal tissues [49, 50, 51]). However, ongoing stem-cell differentiation at this border has the opposite effect by creating more points of contact between the newly

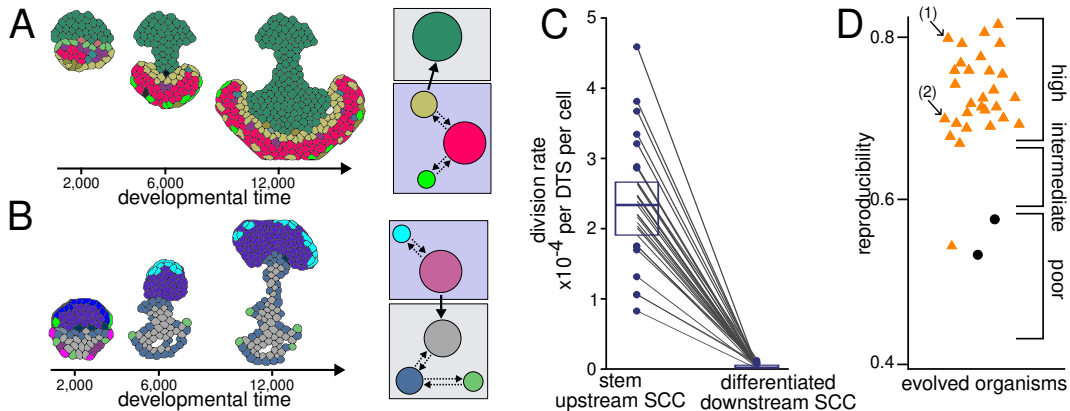


Figure 6: **Reproducible morphogenesis with stem-cell systems is evolutionarily accessible.** **AB** Development of two organism with stem-cell systems. Morphologies are shown after 2,000, 6,000 and 12,000 DTS. A Simplified state space of each organism is shown to the right of their respective developments, indicating multiple SCCs with unidirectional transitions. **C** The rate at which cells divide per developmental time when their state belongs to an upstream SCC (left) or a downstream SCC (right). Each data point represents an SCC from the 29 evolved organisms that had multiple SCCs with unidirectional transitions that were evolved under selection for directional motion and morphological complexity. Black lines connect upstream SCCs to their counterpart downstream SCCs. Boxes show medians and interquartile ranges (IQR). **D** Reproducibility scores for the 31 evolved organisms from simulations selecting for both directional motion and morphological complexity. Black circles indicate organisms with a single SCC. Orange triangles indicate organisms with stem-cell systems. Categories of “high”, “intermediate” and “poor” are copied from Fig. 3C. Numbers (1) and (2) refer to the organisms in panels (B) and (C), respectively.

formed differentiated cells and yet-to-differentiate stem cells, thus increasing adhesion energy. To minimise this adhesion energy, stem cells move away from the points of contacts with the new differentiated cells. Thus, the location-specific differentiation induced by differentiated cells guides the direction of stem-cell motion. Together, these results suggest that interactions between stem and differentiated cells represent another aspect of the morphogenetic division of labour, whereby differentiated cells not only maintain the shape formed by stem cells but also make this shape formation consistent.

A practical implication of our finding that reproducible morphogenesis is a consequence of interactions between stem and differentiated cells is that we should be able to program the same robust morphology by appropriately arranging stem and differentiated cells with different initial conditions. To determine if this is possible, we created arbitrary shapes of stem and differentiated cells and simulated their development. Figure 5I shows an example that begins with a triangular shape of differentiated cells from organism-6 accompanied by a small cluster of type-2 stem cells from that organism on the diagonal surface. This is predicted to result in the stem cells moving diagonally away from the differentiated cells to generate a stalk of differentiated cells in their wake, which is indeed what is observed (Fig. 5I). Similar results were obtained for different initial shapes and different stem-cell systems (Fig. S6HI), demonstrating the robustness of stem-cell system morphogenesis to different initial conditions. These results suggest that repeating or even branching morphologies can be generated by the appropriate initial positioning of stem and differentiated cells, and that these morphologies should be highly reproducible due to the nature of stem-cell system morphogenesis.

## 2.6 Reproducible morphogenesis with stem-cell systems is evolutionarily accessible from most initial conditions

Our results show that stem-cell systems evolved only in a minority of simulations (24 out of the 90 organisms with complex morphologies). We asked whether this is because stem-cell systems are evolutionarily accessible from a restricted portion of genotype space, and thus determined

by the initial conditions, or because they are selectively disfavoured by the particular fitness criterion we used. To address this, we tested an alternative selection criterion that favoured not only the morphological complexity but also the directional motion of organisms. This additional selection for directional motion is expected to favour stem-cell systems because directional motion is a property of morphogenesis with stem-cell systems (Fig. 5F), although it does not directly select for stem-cell systems or reproducibility. We quantified directional motion by determining how much an organism’s centre of mass (measured in pixels) shifts over the 12,000 DTS. We ran 35 simulations lasting at least  $2.5 \times 10^3$  evolutionary generations, of which 31 evolved organisms surpassed our arbitrary fitness threshold (Methods 4.5). We found the great majority of these organisms (29 out of 31) had evolved stem-cell systems (Fig. 6ABC and S7ABCD). Of these 29 organisms, all but one displayed highly reproducible morphogenesis (Fig. 6D). In contrast, the two organisms that did not evolve stem-cell systems displayed poorly reproducible morphogenesis (Fig. 6D and S7E). In addition, we found that stem-cell systems are evolvable when the model assumes simpler gene regulatory networks that lack contractile proteins and have only half the number of the other genes (Fig S7FGH). Together, these results suggest that the evolution of stem-cell systems are robust to the structure of the model, and are likely “easy” to evolve across a wide range of starting genotypes and regulatory networks.

### 3 Discussion

In this study, we found that reproducible morphogenesis evolves in a sizeable fraction of simulations with selection solely for complex morphology, indicating that morphogenetic reproducibility can be an emergent by-product of complex morphogenesis. We show that this reproducibility is realised by a morphogenetic division of labour based on stem-cell systems, where mobile, dividing stem cells “shape” morphologies and irreversibly differentiate into stationary, non-dividing cells that “maintain” these morphologies. This labour division allows differentiated cells to serve as “anchor points” that establish the locations of stem-cell differentiation and directions of stem-cell motion. These locations are made consistent by interactions between stem and differentiated cells mediated by morphogen gradients as well as differential cell adhesion. Thus, we propose that stem-cell systems have a previously unrecognised role in enabling reproducible complex morphogenesis, in addition to their well-known role of generating specialised cell types [2, 52, 53, 54]. This proposal is supported by three key observations that we describe below.

The first observation is that stem-cell-based morphogenesis appears to evolve from most regions of genotype space (Fig. 6). Although all simulations evolved distinct gene regulatory networks (GRNs), each generating a different morphology (i.e., simulations took different evolutionary paths, a well-documented phenomenon in developmental evolution [4, 55, 56]), we found that stem-cell-based morphogenesis evolved repeatedly. This repeated evolution indicates that stem-cell-based morphogenesis is not constrained to just a few “special” GRN. Thus, we suggest that so long as gene regulation, cell adhesion, and cell-cell signalling are in place, such as in all animals and some multicellular microbes such as slime moulds [2, 57], stem-cell-based morphogenesis will be a frequent evolutionary outcome in nature when complex morphogenesis is selected for.

The second observation supporting our proposal is that whenever stem-cell-based morphogenesis evolved in our model, it had three properties that have been shown to elevate morphogenetic reproducibility [27]: (1) boundary-localised differentiation mediated by morphogen signalling, (2) the immobility and non-division of differentiated cells, and (3) differential adhesion between stem and differentiated cells. These properties have been shown to enhance morphogenetic reproducibility by smoothing the boundaries between different cell types [26, 27, 58], with smoother boundaries contributing to a more stable spatial organisation of cell types and, thus, more stable morphogenesis. Indeed, the boundaries between stem and differentiated cells in our

simulated organisms appear to be smooth (Figs. 3A, 5A, 6BC). We also found that these three properties enable differentiated cells to act as anchors that guide consistent stem-cell motion and differentiation, which again enhances morphogenetic reproducibility. These three properties are widespread at cell-type boundaries in extant developmental systems [2, 59, 60, 61, 62, 58], implying they are generic properties of morphogenesis. Critically, we observed these three properties whenever stem-cell-based morphogenesis evolved, despite no direct selection for them. Therefore, stem-cell systems appear to be automatically equipped with these three properties, implying that stem-cell-based morphogenesis will be generally reproducible.

The third observation supporting our proposal is that stem-cell systems enable modular morphogenesis. This modularity arises from the fact that stem-cell-based morphogenesis depends solely on the interactions between stem and differentiated cells (e.g., Fig. 5I) and does not depend on external cues or a specific initial shape. Consequently, stem-cell-based morphogenesis is not limited to creating the elongated or bulge-like shapes that evolved in our model. Instead, these shapes could constitute sub-structures within a more complex morphology, such as organ building blocks, where sub-structures are repeated wherever the appropriate cell-type configuration is present. Intriguingly, the stem-cell-based morphogenesis we observed in our evolved organisms resembles the morphogenesis of sub-structures in a number of extant organisms, such as bilaterian body axis and limb elongation, intestinal crypts and villi, lung alveoli, mammary gland buds, salivary gland buds and kidney tubules [63, 64, 65, 66, 67, 68, 69, 9, 51]. For example, in the kidney, nephron tubule formation begins with the recruitment of mesenchymal progenitor (lineage-restricted stem) cells to a ureteric bud branch [70, 71]. These progenitor cells then undergo division and differentiation into epithelial cells to elongate the nephron, a process driven by signals that originate from already differentiated epithelial cells [72], similar to the signalling between stem and differentiated cells that drives elongation in our evolved organisms. This process is repeated in a modular fashion at many locations in the kidney to generate a large number of nephrons. Although stem-cell system morphogenesis does not produce branching in our model, we hypothesise that branching occurs by combining stem-cell systems with species-specific mechanisms known to be involved in branching, such as polarised cell contractions [73]. The abundance of examples in which modular sub-structures are reminiscent of stem-cell-based morphogenesis, suggests that stem-cell-based morphogenesis is frequently employed in extant developmental systems.

In summary, our results suggest that stem-cell systems are a fundamental developmental phenomenon that, in addition to producing specialised cell types, can underpin multicellular morphogenesis and its reproducibility. Expanding our focus on stem-cell systems from solely cell-type specification to also encompassing morphogenesis has important implications for how we understand the generation and regeneration of tissue morphologies. The programming of tissue morphogenesis *ex vivo*, such as organoids, in an accurate and reproducible way is a critical challenge in synthetic biology [74, 75]. Our findings suggest that a better understanding of the roles the different cell types in stem-cell systems play in morphogenesis will enable us to more effectively manipulate the configuration of these cell types to elevate the accuracy and reproducibility of programmed morphogenesis. Finally, our findings open the possibility that some stem-cell systems originally evolved in animal development for a morphogenetic purpose, with their role in producing specialised cell types emerging as a later exaptation.

## 4 Methods

### 4.1 Cellular Potts Model

Our model extends a Cellular Potts Model (CPM) introduced by Hogeweg (2000) [29]. The CPM dynamics are driven by pixel copying, where repeated random sampling of pixels on grid determines the location of these copies. For each chosen pixel, a random neighbouring pixel

from its Moore neighbourhood is selected as the recipient of the pixel copy. Whether the pixel copy is accepted depends on its effect on the system's energy, denoted as  $H$ , represented by

$$H = \sum_{i,j} J_{ij} + \sum_{i,m} J_{im} + \lambda_V \sum_{\sigma} (v_{\sigma} - V_{\sigma})^2 + \lambda_L^{\sigma} \sum_{\sigma} (l_{\sigma} - L_{\sigma})^2. \quad (1)$$

Here,  $H$  encompasses the total surface energy accumulated from cell-cell adhesion ( $J_{ij}$ ) and cell-medium adhesion ( $J_{im}$ ), which are both determined dynamically as functions of protein concentrations (explained later). The index  $i$  is of pixels at cell boundaries. The index  $j$  is of pixels neighbouring  $i$  that are occupied by a different cell from  $i$ . The index  $m$  is of pixels neighbouring  $i$  that are occupied by the medium. Every pixel on the grid has an associated value,  $\sigma$ , that represents either the cell that occupies that pixel ( $\sigma \geq 1$ ) or the medium ( $\sigma = 0$ ). Each cell  $\sigma$  ( $\sigma \geq 1$ ) with current size  $v_{\sigma}$  (in pixels) is constrained to size  $V_{\sigma}$  with parameter  $\lambda_V$  ( $\lambda_V = 0.5$  for all simulations). The longest axis  $l_{\sigma}$  (in pixels) of each cell is constrained to length  $L_{\sigma}$  with  $\lambda_L^{\sigma}$ .  $V_{\sigma}$ ,  $L_{\sigma}$  and  $\lambda_L^{\sigma}$  are determined dynamically (explained later).

If a pixel copy attempt increases  $H$ , it is accepted with probability  $e^{-\frac{\Delta H}{T}}$ , where  $\Delta H$  is the change in  $H$  made by a pixel copy, and  $T$  is a temperature parameter ( $T = 3$  for all simulations). Otherwise ( $\Delta H \leq 0$ ), the pixel copy attempt is always accepted. One developmental time step (DTS) is complete when the number of pixel copy attempts equals the number of pixels on the grid.

## 4.2 Development

An organism starts as a single cell that undergoes six divisions equally spaced in time over the first 300 DTS. During the first 1,500 DTS (referred to as an equilibration phase),  $J_{ij} = 30$  and  $J_{im} = 40$  for all cells. After the equilibration phase,  $J_{ij}$  and  $J_{im}$  are determined by protein concentrations in the cells (described later). At the beginning of the equilibration phase,  $V_{\sigma}$  is set to the initial size of each of the 64 cells and does not change throughout the equilibration phase. After the equilibration phase, cell growth and shrinkage can occur through modulation of the target cell size,  $V_{\sigma}$ .  $V_{\sigma}$  increases when a cell is stretched, and decreases when a cell is squeezed, as follows. When  $v_{\sigma} \geq V_{\sigma} + 3$ ,  $V_{\sigma}$  is updated such that  $V_{\sigma} = v_{\sigma}$ . When  $v_{\sigma} \leq V_{\sigma} - 16$ ,  $V_{\sigma}$  is updated such that  $V_{\sigma} = v_{\sigma}$ . When the cell volume reaches or exceeds a threshold (i.e.,  $v_{\sigma} \geq 100$ ), the cell undergoes division perpendicular to its longest axis. One daughter cell retains the same index  $\sigma$  as the mother cell, while the other daughter cell is assigned a new index  $\sigma'$ . After division, the target area of the daughter cells are  $V_{\sigma} = v_{\sigma}$  and  $V_{\sigma'} = v_{\sigma'}$ . Protein concentrations remain unchanged during upon cell division. If  $v_{\sigma} = 0$ , the cell dies.

## 4.3 Gene regulatory network and morphogens

In each cell  $\sigma$ , there are  $N$  genes, indexed by  $p$ , that each encode a protein whose intracellular concentration is denoted by  $x_p^{\sigma}$ . With the exception of  $p = 1, 2, 3$  (which are morphogens, described later), the following equation determines the change in  $x_p^{\sigma}$  over time  $t$ :

$$\frac{dx_p^{\sigma}}{dt} = \frac{a}{1 + e^{-\beta f_p(x)}} - bx_p^{\sigma} \quad (2)$$

with one unit of  $t$  being one DTS. The first term on the right-hand side represents the increase in  $x_p^{\sigma}$  due to gene expression, and is a sigmoidal function that depends on the regulation by transcription factors ( $f_p(x)$  is explained subsequently) with a maximum production rate  $a$  and large  $\beta$  ( $= 20$ ). The second term represents protein decay with rate  $b$ . We set  $a = b$  for all  $p$ , so  $x_p^{\sigma}$  equilibrates at 1 if the gene is constantly expressed or 0 if it is constantly not expressed. The values of  $a$  and  $b$  are small (specifically,  $6.25 \times 10^{-3}$ ) to assume that the timescale of gene expression is slower than the timescale of CPM dynamics. Numerical integration of Equation 2

occurs with  $\Delta t = 40$  via the Euler method. We chose this value of  $\Delta t$  instead of a smaller value to improve computational speed. The value of  $\Delta t$  can be large because  $a$  and  $b$  are very small. The initial concentrations are  $x_p^\sigma = 1$  for transcription factors (except for maternal factors, which are either  $x_p^\sigma = 1$  or  $x_p^\sigma = 0$  depending on  $\sigma$  at the four-cell stage), and  $x_p^\sigma = 0$  for all other proteins (described later). Integration of Equation 2 begins after the four-cell stage is reached (100 DTS), which is when the asymmetric distribution of maternal factors occurs.

Function  $f_p(x)$  in Equation 2 sums the regulatory effects of  $n = 9$  transcription factors (TFs, which include two maternal factors and three morphogens) as follows:

$$f_p(x) = \left[ \sum_{p'}^n Z_{pp'} x_{p'}^\sigma \right] + \theta \quad (3)$$

where  $Z_{pp'}$  is the regulatory effect of TF encoded by gene  $p'$  on the expression of gene  $p$  ( $Z_{pp'} \in \{0, \pm 1, \pm 2\}$ ). The TF encoded by  $p'$  activates the expression of  $p$  if  $Z_{pp'} > 0$ , inhibits if  $Z_{pp'} < 0$  and has no effect if  $Z_{pp'} = 0$ . The parameter  $\theta$  sets the base level of gene expression.  $\theta = -0.3$  for all simulations, so protein concentrations equilibrate at 0 when they are not regulated by any TFs.

To model cell-cell signalling, the first three ( $p = 1, 2, 3$ ) of the nine transcription factors (TFs) are morphogens. These morphogens diffuse between cells and into the surrounding medium. The concentration of morphogen  $p$  on pixel  $i$  on the grid,  $x_p^i$ , is determined by the following coupled ODE:

$$\frac{dx_p^i}{dt} = D\nabla^2 x_p^i + \omega H(\sigma - 1) x_{N-p}^\sigma - \eta x_p^i \quad (4)$$

where  $D$  is a diffusion constant,  $\omega$  is a production rate,  $\eta$  is a decay rate and  $H(\sigma - 1)$  is the Heaviside step function that evaluates to one if  $\sigma \geq 1$  at pixel  $i$  (the pixel is occupied by a cell) and zero if  $\sigma = 0$  (the pixel is medium). The concentration  $x_{N-p}^\sigma$  represents a signalling protein that activates the expression of one morphogen. The concentration of the three signalling proteins is determined by Equation 2. The operator  $\nabla^2 x_p^i$  is the Laplacian acting on  $x_p^i$ , which, in this context, is the difference between  $x_p^i$  and the average  $x_p^i$  in its von Neumann neighbourhood (i.e., four nearest-neighbouring pixels) divided by a space step  $dx$ , with  $dx = 1/250$  (250 is the length of the square grid in pixels). Numerical integration for Equation 4 occurs with  $\Delta t = 1$  and is performed separately from Equation 2. Equation 4 is subject to the initial condition  $x_p^i = 0$  for all  $i$  and  $p$ . The pixels at the boundary of the grid are subject to  $x_i^p = 0$  for all  $t$  and  $p$ . The constants  $D = 8 \times 10^{-7}$ ,  $\omega = 2.4 \times 10^{-3}$  and  $\eta = 2 \times 10^{-3}$  were used for all simulations and are the same for all three morphogens. We chose these values for two reasons. The first is so that the maximum concentration is approximately 1 and thus similar to the concentrations of TFs per Equation 2. The second is so that the characteristic diffusion length,  $\sqrt{D/\eta} dx$ , is similar to that of a paracrine morphogen, such as Wnts, which signal only to nearby cells [43, 76]. This characteristic diffusion length is five pixels, which is approximately the diameter of a cell. Since  $x_p^i$  regulates genes in each cell  $\sigma$ , we average  $x_p^i$  over all  $i$  with the value  $\sigma$  to obtain  $x_p^\sigma$ . During the equilibration period (DTS < 1500), the parameters  $D, \omega, \eta$  and  $\Delta t$  are multiplied by eight in order to speed up the time taken for morphogens to reach a steady state. The faster timescale does not have an effect on morphogenesis because there is no morphogenesis during the equilibration phase.

#### 4.4 Adhesion and contractile proteins

Cells encode 15 adhesion proteins constituting five pairs of lock-and-key proteins that determine cell-cell adhesion and five medium proteins that determine cell adhesion to the extracellular medium. Each lock protein has a complementary key protein to which it can bind. When two cells are in contact, the adhesion energy between them ( $J_{ij}$  in Equation 1) decreases with the



number of expressed pairs of compatible locks and keys. Each pair of lock and key reduces adhesion energy by the same amount. The adhesion energy to the extracellular medium ( $J_{im}$  in Equation 1) decreases with the number of medium proteins expressed by a cell. Medium proteins have graded adhesion strengths (described subsequently). Adhesion protein concentrations are booleanised to an ON or OFF state for adhesion energy calculations (i.e., ON if  $x_p^\sigma > 0.5$  else OFF). Specifically,  $J_{ij}$  between neighbouring pixels  $i$  and  $j$  that belong to different cells is:

$$J_{ij} = J_{ij}^{\max} - 2 \sum_{k=1}^5 [\phi_k^{ij} + \phi_k^{ji}] \quad (5)$$

where  $\phi_k^{ij} = 1$  if the  $k$ -th lock in the cell of pixel  $i$  and the  $k$ -th key in the cell of pixel  $j$  are both ON and otherwise  $\phi_k^{ij} = 0$ . Similarly,  $J_{im}$  between pixels  $i$  and  $m$  belonging to a cell and the medium, respectively, is:

$$J_{im} = J_{im}^{\max} - \sum_{k=1}^5 k\psi_k \quad (6)$$

where  $\psi_k = 1$  if the  $k$ -th medium-adhesion protein is ON, and otherwise  $\psi_k = 0$ .  $J_{ij}^{\max} = 24$  and  $J_{im}^{\max} = 21$  for all simulations. In Figure S8ABCD, we show that the morphogenesis of evolved organisms is not disrupted by changes to these parameters.

Cells encode two contractile proteins that make the cell shape less deformable by energetically constraining it to an elliptic shape. Cell shapes are defined as ellipses that have a major axis of length  $l_\sigma$  constrained to a target length of  $L_\sigma$  with  $\lambda_L^\sigma$  (see Equation 1).  $L_\sigma$  increases with the number of expressed contractile proteins. Contractile proteins are first booleanised to an ON or OFF state by the same method used for adhesion proteins. When one length protein is ON in cell  $\sigma$ ,  $L_\sigma$  is set to one-sixth of  $v_\sigma$ ; When two are ON,  $L_\sigma$  is set to one-third of  $v_\sigma$  (these numbers are arbitrarily chosen). To implement the presence or absence of a length constraint depending on whether contractile proteins are expressed, we set  $\lambda_L^\sigma = 0.1$  if either contractile protein in cell  $\sigma$  is ON, otherwise  $\lambda_L^\sigma = 0$ .

## 4.5 Evolution

To simulate the evolution of morphogenesis, we established an initial population of 60 organisms with each assigned a different GRN and developing on a separate CPM grid. Each GRN is specified by 234  $Z_{pp'}$  values representing the regulatory effects of all transcription factors, as described in Equation 3 (nine transcription factors regulate 26 genes including themselves). The  $Z_{pp'}$  values of the GRNs assigned to the initial population are randomly generated according to the following probabilities:  $P(Z_{pp'} = 0) = 0.54$ ,  $P(Z_{pp'} = 1) = 0.18$ ,  $P(Z_{pp'} = -1) = 0.18$ ,  $P(Z_{pp'} = 2) = 0.05$  and  $P(Z_{pp'} = -2) = 0.05$ . The 15 organisms with the highest morphological complexity reproduce four times to populate the next generation (the definition of morphological complexity is described in the next paragraph). Upon reproduction, there is a 50% chance that one of the  $Z_{pp'}$  values in the GRN mutates. The specific  $Z_{pp'}$  that mutates is chosen at random with equal probability. The mutation alters the value of  $Z_{pp'}$ , independent of its current value, according to same probabilities used to generate the  $Z_{pp'}$  assigned to the initial population. Gene duplication and deletion do not occur.

Morphological complexity was defined based on an algorithm that quantifies the complexity of two-dimensional shapes [77]. Morphological complexity is a summation of two measures: the deviation of morphology from a circle (denoted by  $z_1$ ) and the degree of inward folds (denoted by  $z_2$ ), as described below.

The deviation of morphology from a circle  $z_1$  is defined by the following equation:

$$z_1 = \langle |r_c - r(\theta)| \rangle_\theta \quad (7)$$

where  $r_c$  is the hypothetical radius of an organism if the organism’s morphology were perfectly circular, and  $r(\theta)$  is the maximum distance from the centre of mass of the organism to any pixel in the direction specified by angle  $\theta$  (one pixel corresponds to one unit mass). The notation  $\langle \dots \rangle_\theta$  indicates an average taken over all angles  $\theta$ , where  $\theta$  is discretised into 360 degrees for computation.

The degree of inward folds ( $z_2$ ) measures the sum of the sizes of regions of the medium surrounded by concave parts of an organism. To identify these regions, we begin by drawing horizontal parallel lines across the CPM grid spaced one pixel apart, resulting in a total of 250 lines. Next, we locate segments along the lines that intersect the extracellular medium in between cells. The segments were discarded if they did not exceed a minimum length of 20 pixels to filter out inward folds due to stochastic cell boundary fluctuations. The number of the retained segments was recorded. The above procedure was repeated by tilting the 250 parallel lines at 12 evenly-spaced angles across the range  $[-\pi/2, \pi/2]$ .  $z_2$  is defined as the square root of the total number of the retained segments ( $z_2$  is independent of the lengths of the retained segments).

Morphological complexity was defined as  $2z_1 + 2.5z_2$ . The weights of 2 and 2.5 were selected to ensure that the maximum value of either term is approximately 100 for shapes that are realistically achievable within this model, ensuring that neither term dominates the fitness criterion. In order to filter out noise, morphological complexity is taken as an average of 10 evenly-spaced measurements over the last 1,000 DTS. If cells lose physical contact with other cells during development (see Fig. S8EF for examples), we assign the organism a fitness of 0 as our quantification of morphological complexity was not designed to handle multiple shapes.

The alternative fitness criterion that was used to determine whether stem-cell-based morphogenesis is evolutionary accessible was implemented in two stages. In the first stage, the fitness criterion is the displacement of an organism’s centre of mass, measured in pixels, from the start to the end of the 12,000 DTS, denoted  $z_3$ . Once the average fitness across all organisms in a population exceeded 15 pixels, the fitness criterion transitioned to the second stage. In the second stage, the fitness criterion is  $(2z_1 + 2.5z_2)/2 + z_3^{1.5}$ . The weightings of each criterion were selected so that the maximum value of each is approximately 100 for shapes that are realistically achievable within this model, ensuring that neither term dominates the fitness criterion.

To determine whether an evolutionary simulation succeeded or failed, we used fitness thresholds. The thresholds were applied to the organism that recorded the most complex morphology in the final generation of the simulation. In the simulations selecting only for morphological complexity, we applied a threshold of 70 after averaging the morphological complexity over 60 developmental replicates in order to account for variance in the complexity score. However, this threshold does not affect our key findings, as there are still highly reproducible organisms with stem-cell systems below the threshold (See Fig. S2AB). In the simulations selecting for both shifting centre of mass and morphological complexity, the fitness threshold we used to determine whether an evolutionary simulation succeeded was whether the second stage was reached.

## 4.6 Cell state and state space

The cell state is an  $n$ -dimensional boolean vector, where  $n$  is the total number of adhesion and contractile proteins (although the results do not change when TFs are included in the vector as well). Each element in this vector is the concentration of each protein booleanised to either ON or OFF (as described previously for lock, key and contractile proteins). Each boolean vector is assigned a single colour on the CPM grid. These colours are chosen arbitrarily, and each organism has its own distinct colour set. While this approach means that the same cell state might appear in different colours across organisms, it is uncommon to encounter identical

cell states in different evolved organisms. The cell state of each cell is determined after every numerical integration step of Equation 2. A change in a cell’s boolean vector corresponds to a cell state transition.

To generate the cell state space, we recorded all cell state transitions for all cells after 6,000 DTS from the beginning of development. Although it makes no qualitative difference when the recording of transitions begins, starting at 6,000 reduces the appearance of “transient” cell states [78], such as the cell state corresponding to the initial conditions of cell proteins, which makes it easier to visualise the cell state space. Cell state transitions are recorded from 10 developmental replicates in order to reduce the effect of noise on cell state space creation. The state space is the directed graph, where the nodes are the cell states and the edges are the transitions. Figure S4IJ shows two examples of these directed graphs. To simplify the graph, we prune rare transitions (those that occur less than five times across all cells per developmental replicate) and rare cell states. To identify rare cell states, we first count the number of cells in each state after each integration step of Equation 2 to obtain a frequency distribution of cell states. Rare cell states are those that have a frequency of less than 1% from the 10 developmental replicates. However, even without any pruning of cell state transitions and cell states, the cell state space of 22 out of 24 organisms designated as having stem-cell systems still exhibit irreversible differentiation (Fig. S8GHIJ shows one that does not follow this rule).

We used a depth-first search algorithm to identify a graph’s strongly connected components (SCCs). Irreversible differentiation occurs when there is weak connectivity between SCCs (i.e., a path exists from SCC  $u$  to SCC  $v$ , but not  $v$  to  $u$ ). SCCs that do not have incoming paths from any other SCCs (source components) are designated as stem-cell types. SCCs that have no outgoing paths to any other SCCs are designated as differentiated-cell types.

## 4.7 Reproducibility score

We measured the morphogenetic reproducibility of organisms in a rotation-, reflection- and translation-invariant manner, as follows. We first replayed the development of an organism 60 times with different random seeds. We then performed pairwise comparisons of all developed morphologies ( $60 \times 59/2$  comparisons). For each pair of morphologies, we computed morphological similarity scores between the two CPM grids on which morphologies developed (denoted by  $A$  and  $B$ ). We computed the morphological similarity scores (denoted  $\text{Jac}$ ) over many rotations, reflections and translations of grid  $B$  relative to a fixed grid  $A$  to find the maximum possible similarity between them (denoted  $\text{Jac}_{\max}$ ).

To calculate  $\text{Jac}$ , grids  $A$  and  $B$  are transformed from Cartesian to polar coordinates, as follows. The polar coordinate  $(r, \theta)$  is discretised into  $250 \times 360$  pixels. Each pixel in  $(r, \theta)$  is mapped to the pixel closest to  $(r \cos \theta, r \sin \theta)$  in  $A$  or  $B$ , where  $r$  is the distance from the midpoint of grid  $A$  or one of 25 equally-spaced locations in grid  $B$  (thus, multiple pixels in the polar coordinate can be mapped to the same pixel in the Cartesian coordinate). Let  $A_\theta^r$  and  $B_\theta^r$  be one if the mapped pixel in  $A$  or  $B$  belongs to a biological cell and 0 otherwise. We then calculated the Jaccard index,  $\text{Jac}(A_\theta^r, B_\theta^r)$ , which measures the similarity between  $A_\theta^r$  and  $B_\theta^r$ , as follows:

$$\text{Jac}(A_\theta^r, B_\theta^r) = \frac{A_\theta^r \cap B_\theta^r}{A_\theta^r \cup B_\theta^r} \quad (8)$$

where  $A_\theta^r \cap B_\theta^r = \sum_{\theta=0^\circ}^{359^\circ} \sum_{r=0}^{249} r \delta(A_\theta^r, 1) \delta(B_\theta^r, 1)$  is the number of pixels in the polar coordinate with a value of one (i.e., the pixel is occupied by a cell) on both  $A_\theta^r$  and  $B_\theta^r$ , where  $\delta$  is the Kronecker delta. The multiplication by  $r$  accounts for the fact that the length of an arc drawn by an increment in  $\theta$  increases as  $r$  increases. Similarly,  $A_\theta^r \cup B_\theta^r = \sum_{\theta=0^\circ}^{359^\circ} \sum_{r=0}^{249} r [\delta(A_\theta^r, 1) + \delta(B_\theta^r, 1) - \delta(A_\theta^r, B_\theta^r)]$  is the number of pixels in the polar coordinate in which  $A_\theta^r = 1$  or  $B_\theta^r = 1$  (or both). Thus, when  $A_\theta^r$  and  $B_\theta^r$  are exactly the same,  $\text{Jac}(A_\theta^r, B_\theta^r) = 1$ . Next, we shift all

values of  $B_\theta^r$  to  $B_{\theta+1 \pmod{360}}^r$ , corresponding to a one-degree rotation in Cartesian coordinates, and compute  $\text{Jac}(A_\theta^r, B_\theta^r)$  again. We repeat these one-degree rotations 360 times, computing  $\text{Jac}(A_\theta^r, B_\theta^r)$  for each. Next, we invert all values of  $B_\theta^r$  to  $B_{180-\theta \pmod{360}}^r$ , which corresponds to a reflection of grid  $B$ , and repeat the 360 one-degree rotations again, computing  $\text{Jac}(A_\theta^r, B_\theta^r)$  for each. Furthermore, we repeated these 720 computations for 25 equally-spaced translations of grid  $B$  (as mentioned previously), achieved by shifting the location on grid  $B$  chosen to be  $r = 0$  for the polar coordinate. Translations occur in steps of five pixels at a time to make up a five-by-five square. The maximum  $\text{Jac}(A_\theta^r, B_\theta^r)$  recorded across all rotation, reflections and translations for each pairwise comparison is the maximum possible similarity, denoted  $\text{Jac}_{\max}$ . The reproducibility score for an organism is the average  $\text{Jac}_{\max}$  across all  $60 \times 59/2$  pairwise comparisons.

## 4.8 Momentum and anisotropy

The momentum,  $p_\sigma(t)$ , of cell  $\sigma$  at time  $t$  (where  $t$  is in DTS) was defined as the distance travelled by the cell's centre of mass between  $t - t_w$  and  $t$  multiplied by the cell's mass at  $t - t_w/2$ , with unit mass represented by one pixel:

$$p_\sigma(t) = m_\sigma \left( t - \frac{t_w}{2} \right) \frac{s_\sigma(t) - s_\sigma(t - t_w)}{t_w} \quad (9)$$

where  $s_\sigma(t)$  is the cell's centre of mass,  $m_\sigma(t)$  is the cell's mass at  $t$ , and  $t_w$  is the waiting time. The waiting time  $t_w$  was set to 500 to average out the influence of stochastic membrane fluctuations and cell divisions on the centre of mass of the cell, thereby capturing the true mobility of cells. If a cell divides during the waiting time and the  $\sigma$  values of the parent and daughter cells differ, Equation 9 is modified by subtracting the position of the parent cell's  $\sigma$  centre of mass ( $s_\sigma(t - t_w)$ ) from the daughter cell's  $\sigma'$  centre of mass ( $s_{\sigma'}(t)$ ).

In order to separate cell momentum by SCC, we first connected each recording of cell momentum  $p_\sigma(t)$  to the state of the cell at  $t - \frac{t_w}{2}$ . We then assigned each momentum recording into an SCC depending on that cell state. To create the polar plots of cell momentum magnitude (Fig. 5DE), we categorised each momentum measurement assigned to an SCC into one of 36 bins based on its direction. Each bin encompasses momentum measurements within an angular width of  $10^\circ$ . To measure anisotropic motion (Fig. 5FGH), we calculated the variance across these 36 bins. To account for total momentum, we divided the variance by the mean momentum across the 36 bins, equal to the dispersion index. The anisotropy value for an SCC is the average of the dispersion indices across five developmental replicates.

## References

- [1] Brigid LM Hogan. Morphogenesis. *Cell*, 96(2):225–233, 1999.
- [2] Lewis Wolpert, Cheryll Tickle, and Alfonso Martinez Arias. *Principles of Development*. Oxford University Press, USA, 2015.
- [3] Brian C Goodwin, Stuart Kauffman, and JD Murray. Is morphogenesis an intrinsically robust process? *Journal of Theoretical Biology*, 163(1):135–144, 1993.
- [4] Stuart A Kauffman et al. *The origins of order: Self-organization and selection in evolution*. Oxford University Press, USA, 1993.
- [5] Diethard Tautz. Segmentation. *Developmental Cell*, 7(3):301–312, 2004.
- [6] Merlijn Staps, Pearson W Miller, Corina E Tarnita, and Ricardo Mallarino. Development shapes the evolutionary diversification of rodent stripe patterns. *Proceedings of the National Academy of Sciences*, 120(45):e2312077120, 2023.

- [7] Aimée Zuniga. Next generation limb development and evolution: old questions, new perspectives. *Development*, 142(22):3810–3820, 2015.
- [8] M Luisa Iruela-Arispe and Greg J Beitel. Tubulogenesis. *Development*, 140(14):2851–2855, 2013.
- [9] Yuchuan Miao, Yannis Djeffal, Alessandro De Simone, Kongju Zhu, Jong Gwan Lee, Ziqi Lu, Andrew Silberfeld, Jyoti Rao, Oscar A Tarazona, Alessandro Mongera, et al. Reconstruction and deconstruction of human somitogenesis in vitro. *Nature*, 614(7948):500–508, 2023.
- [10] Aristotle. *The complete works of Aristotle—The revised Oxford translation*. Princeton University Press, 1984.
- [11] Marie-Anne Félix and Michalis Barkoulas. Pervasive robustness in biological systems. *Nature Reviews Genetics*, 16(8):483–496, 2015.
- [12] Rebecca M Green, Jennifer L Fish, Nathan M Young, Francis J Smith, Benjamin Roberts, Katie Dolan, Irene Choi, Courtney L Leach, Paul Gordon, James M Cheverud, et al. Developmental nonlinearity drives phenotypic robustness. *Nature Communications*, 8(1):1970, 2017.
- [13] Marco Osterwalder, Iros Barozzi, Virginie Tissières, Yoko Fukuda-Yuzawa, Brandon J Mannion, Sarah Y Afzal, Elizabeth A Lee, Yiwen Zhu, Ingrid Plajzer-Frick, Catherine S Pickle, et al. Enhancer redundancy provides phenotypic robustness in mammalian development. *Nature*, 554(7691):239–243, 2018.
- [14] Peter S Swain, Michael B Elowitz, and Eric D Siggia. Intrinsic and extrinsic contributions to stochasticity in gene expression. *Proceedings of the National Academy of Sciences*, 99(20):12795–12800, 2002.
- [15] Lev S Tsimring. Noise in biology. *Reports on Progress in Physics*, 77(2):026601, 2014.
- [16] James Briscoe and Stephen Small. Morphogen rules: design principles of gradient-mediated embryo patterning. *Development*, 142(23):3996–4009, 2015.
- [17] Edmund J Crampin, Eamonn A Gaffney, and Philip K Maini. Reaction and diffusion on growing domains: scenarios for robust pattern formation. *Bulletin of Mathematical Biology*, 61(6):1093–1120, 1999.
- [18] Matthew Freeman. Feedback control of intercellular signalling in development. *Nature*, 408(6810):313–319, 2000.
- [19] Avigdor Eldar, Ruslan Dorfman, Daniel Weiss, Hilary Ashe, Ben-Zion Shilo, and Naama Barkai. Robustness of the bmp morphogen gradient in drosophila embryonic patterning. *Nature*, 419(6904):304–308, 2002.
- [20] Hiroaki Kitano. Biological robustness. *Nature Reviews Genetics*, 5(11):826–837, 2004.
- [21] Katherine W Rogers and Alexander F Schier. Morphogen gradients: from generation to interpretation. *Annual Review of Cell and Developmental Biology*, 27:377–407, 2011.
- [22] Asakiran Madamanchi, Mary C Mullins, and David M Umulis. Diversity and robustness of bone morphogenetic protein pattern formation. *Development*, 148(7):dev192344, 2021.
- [23] J Reinitz, S Vakulenko, I Sudakow, and D Grigoriev. Robust morphogenesis by chaotic dynamics. *Scientific Reports*, 13(1):1–9, 2023.
- [24] Maciej Majka, Nils B Becker, Pieter Rein ten Wolde, Marcin Zagorski, and Thomas R Sokolowski. Stable developmental patterns of gene expression without morphogen gradients. *PLoS computational biology*, 20(12):e1012555, 2024.

- [25] Darren Gilmour, Martina Rembold, and Maria Leptin. From morphogen to morphogenesis and back. *Nature*, 541(7637):311–320, 2017.
- [26] Pascal F Hagolani, Roland Zimm, Miquel Marin-Riera, and Isaac Salazar-Ciudad. Cell signaling stabilizes morphogenesis against noise. *Development*, 146(20):dev179309, 2019.
- [27] Hugo Cano-Fernández, Tazzio Tissot, Miguel Brun-Usan, and Isaac Salazar-Ciudad. On the origins of developmental robustness: modeling buffering mechanisms against cell-level noise. *Development*, 150(24):dev201911, 2023.
- [28] Paulien Hogeweg. On searching generic properties of non-generic phenomena: an approach to bioinformatic theory formation. In *Artificial life VI*, pages 285–294. MIT Press Cambridge, MA, 1998.
- [29] Paulien Hogeweg. Evolving mechanisms of morphogenesis: on the interplay between differential adhesion and cell differentiation. *Journal of Theoretical Biology*, 203(4):317–333, 2000.
- [30] Paulien Hogeweg. Shapes in the shadow: Evolutionary dynamics of morphogenesis. *Artificial Life*, 6(1):85–101, 2000.
- [31] François Graner and James Glazier. Simulation of biological cell sorting using a two-dimensional extended potts model. *Physical Review Letters*, 69(13):2013, 1992.
- [32] Tsuyoshi Hirashima, Elisabeth G Rens, and Roeland MH Merks. Cellular potts modeling of complex multicellular behaviors in tissue morphogenesis. *Development, Growth & Differentiation*, 59(5):329–339, 2017.
- [33] Tania Rozario and Douglas W DeSimone. The extracellular matrix in development and morphogenesis: a dynamic view. *Developmental Biology*, 341(1):126–140, 2010.
- [34] Paul C Bressloff. *Stochastic Processes in Cell Biology*, volume 41. Springer, 2014.
- [35] Christopher S Chen, Milan Mrksich, Sui Huang, George M Whitesides, and Donald E Ingber. Geometric control of cell life and death. *Science*, 276(5317):1425–1428, 1997.
- [36] Celeste M Nelson, Ronald P Jean, John L Tan, Wendy F Liu, Nathan J Sniadecki, Alexander A Spector, and Christopher S Chen. Emergent patterns of growth controlled by multicellular form and mechanics. *Proceedings of the National Academy of Sciences*, 102(33):11594–11599, 2005.
- [37] Charlène Guillot and Thomas Lecuit. Mechanics of epithelial tissue homeostasis and morphogenesis. *Science*, 340(6137):1185–1189, 2013.
- [38] Johannes F Knabe, Maria J Schilstra, and Chrystopher L Nehaniv. Evolution and morphogenesis of differentiated multicellular organisms: autonomously generated diffusion gradients for positional information. *Artificial Life XI*, 2008.
- [39] Enrico Sandro Colizzi, Renske MA Vroomans, and Roeland MH Merks. Evolution of multicellularity by collective integration of spatial information. *Elife*, 9:e56349, 2020.
- [40] Shreyas U Hirway, Christopher A Lemmon, and Seth H Weinberg. Multicellular mechanochemical hybrid cellular potts model of tissue formation during epithelial-mesenchymal transition. *Computational and Systems Oncology*, 1(4):e1031, 2021.
- [41] Renske MA Vroomans and Enrico Sandro Colizzi. Evolution of selfish multicellularity: collective organisation of individual spatio-temporal regulatory strategies. *BMC Ecology and Evolution*, 23(1):35, 2023.

- [42] Benjamin L Martin and David Kimelman. Canonical wnt signaling dynamically controls multiple stem cell fate decisions during vertebrate body formation. *Developmental Cell*, 22(1):223–232, 2012.
- [43] Henner F Farin, Ingrid Jordens, Mohammed H Mosa, Onur Basak, Jeroen Korving, Daniele VF Tauriello, Karin De Punder, Stephane Angers, Peter J Peters, Madelon M Maurice, et al. Visualization of a short-range wnt gradient in the intestinal stem-cell niche. *Nature*, 530(7590):340–343, 2016.
- [44] Hui Ting Zhang and Takashi Hiiragi. Symmetry breaking in the mammalian embryo. *Annual Review of Cell and Developmental Biology*, 34:405–426, 2018.
- [45] Malcolm S Steinberg. Differential adhesion in morphogenesis: a modern view. *Current Opinion in Genetics & Development*, 17(4):281–286, 2007.
- [46] Ivonne M Sehring, Bo Dong, Elsa Denker, Punit Bhattachan, Wei Deng, Birthe T Mathiesen, and Di Jiang. An equatorial contractile mechanism drives cell elongation but not cell division. *PLOS Biology*, 12(2):e1001781, 2014.
- [47] Scott F Gilbert. *Developmental Biology*. sinauer associates, Inc, 2010.
- [48] Chikara Furusawa and Kunihiko Kaneko. Theory of robustness of irreversible differentiation in a stem cell system: chaos hypothesis. *Journal of Theoretical Biology*, 209(4):395–416, 2001.
- [49] Pierre-Gilles De Gennes. Wetting: statics and dynamics. *Reviews of Modern Physics*, 57(3):827, 1985.
- [50] Carlos Pérez-González, Ricard Alert, Carles Blanch-Mercader, Manuel Gómez-González, Tomasz Kolodziej, Elsa Bazellieres, Jaume Casademunt, and Xavier Trepat. Active wetting of epithelial tissues. *Nature Physics*, 15(1):79–88, 2019.
- [51] Tyler R Huycke, Teemu J Häkkinen, Hikaru Miyazaki, Vasudha Srivastava, Emilie Barruet, Christopher S McGinnis, Ali Kalantari, Jake Cornwall-Scoones, Dedeepya Vaka, Qin Zhu, et al. Patterning and folding of intestinal villi by active mesenchymal dewetting. *Cell*, 187(12):3072–3089, 2024.
- [52] Irving L Weissman. Stem cells: units of development, units of regeneration, and units in evolution. *Cell*, 100(1):157–168, 2000.
- [53] Thibaut Brunet and Nicole King. The origin of animal multicellularity and cell differentiation. *Developmental Cell*, 43(2):124–140, 2017.
- [54] Claudio Collinet and Thomas Lecuit. Programmed and self-organized flow of information during morphogenesis. *Nature Reviews Molecular Cell Biology*, 22(4):245–265, 2021.
- [55] Isaac Salazar-Ciudad and Miquel Marín-Riera. Adaptive dynamics under development-based genotype–phenotype maps. *Nature*, 497(7449):361–364, 2013.
- [56] Christian Peter Klingenberg. Evolution and development of shape: integrating quantitative approaches. *Nature Reviews Genetics*, 11(9):623–635, 2010.
- [57] Joan E Strassmann, Yong Zhu, and David C Queller. Altruism and social cheating in the social amoeba dictyostelium discoideum. *Nature*, 408(6815):965–967, 2000.
- [58] Kosuke Mizuno, Tsuyoshi Hirashima, and Satoshi Toda. Robust tissue pattern formation by coupling morphogen signal and cell adhesion. *EMBO Reports*, pages 1–24, 2024.
- [59] Thomas Lecuit and Pierre-Francois Lenne. Cell surface mechanics and the control of cell shape, tissue patterns and morphogenesis. *Nature Reviews Molecular Cell Biology*, 8(8):633–644, 2007.

- [60] Takayoshi Inoue, Taro Tanaka, Masatoshi Takeichi, Osamu Chisaka, Shun Nakamura, and Noriko Osumi. Role of cadherins in maintaining the compartment boundary between the cortex and striatum during development. *Development*, 128(4):561–569, 2001.
- [61] Anna Kicheva, Tobias Bollenbach, Ana Ribeiro, Helena Pérez Valle, Robin Lovell-Badge, Vasso Episkopou, and James Briscoe. Coordination of progenitor specification and growth in mouse and chick spinal cord. *Science*, 345(6204):1254927, 2014.
- [62] Oriol Canela-Xandri, Francesc Sagués, Jaume Casademunt, and Javier Buceta. Dynamics and mechanical stability of the developing dorsoventral organizer of the wing imaginal disc. *PLoS Computational Biology*, 7(9):e1002153, 2011.
- [63] Brooke J Damon, Nadejda V Mezentseva, Jaliya S Kumaratilake, Gabor Forgacs, and Stuart A Newman. Limb bud and flank mesoderm have distinct “physical phenotypes” that may contribute to limb budding. *Developmental Biology*, 321(2):319–330, 2008.
- [64] Jason R Rock and Brigid LM Hogan. Epithelial progenitor cells in lung development, maintenance, repair, and disease. *Annual Review of Cell and Developmental Biology*, 27:493–512, 2011.
- [65] Toshiro Sato and Hans Clevers. Growing self-organizing mini-guts from a single intestinal stem cell: mechanism and applications. *Science*, 340(6137):1190–1194, 2013.
- [66] Jun Yang and Jichao Chen. Developmental programs of lung epithelial progenitors: a balanced progenitor model. *Wiley Interdisciplinary Reviews: Developmental Biology*, 3(5):331–347, 2014.
- [67] Nikolce Gjorevski and Celeste M Nelson. Integrated morphodynamic signalling of the mammary gland. *Nature Reviews Molecular Cell Biology*, 12(9):581–593, 2011.
- [68] Colinda LGJ Scheele, Edouard Hannezo, Mauro J Muraro, Anoek Zomer, Nathalia SM Langedijk, Alexander Van Oudenaarden, Benjamin D Simons, and Jacco Van Rheenen. Identity and dynamics of mammary stem cells during branching morphogenesis. *Nature*, 542(7641):313–317, 2017.
- [69] Shaohe Wang, Kazue Matsumoto, Samantha R Lish, Alexander X Cartagena-Rivera, and Kenneth M Yamada. Budding epithelial morphogenesis driven by cell-matrix versus cell-cell adhesion. *Cell*, 184(14):3702–3716, 2021.
- [70] Akio Kobayashi, M Todd Valerius, Joshua W Mugford, Thomas J Carroll, Michelle Self, Guillermo Oliver, and Andrew P McMahon. Six2 defines and regulates a multipotent self-renewing nephron progenitor population throughout mammalian kidney development. *Cell Stem Cell*, 3(2):169–181, 2008.
- [71] Jack Schnell, MaryAnne Achieng, and Nils Olof Lindström. Principles of human and mouse nephron development. *Nature Reviews Nephrology*, 18(10):628–642, 2022.
- [72] Andrew P McMahon. Development of the mammalian kidney. *Current Topics in Developmental Biology*, 117:31–64, 2016.
- [73] Victor D Varner and Celeste M Nelson. Cellular and physical mechanisms of branching morphogenesis. *Development*, 141(14):2750–2759, 2014.
- [74] Meritxell Huch, Juergen A Knoblich, Matthias P Lutolf, and Alfonso Martinez-Arias. The hope and the hype of organoid research. *Development*, 144(6):938–941, 2017.
- [75] N Gjorevski, M Nikolaev, TE Brown, O Mitrofanova, N Brandenburg, FW DelRio, FM Yavitt, P Liberali, KS Anseth, and MP Lutolf. Tissue geometry drives deterministic organoid patterning. *Science*, 375(6576):eaaw9021, 2022.



- [76] Stephen Kerridge, Akankshi Munjal, Jean-Marc Philippe, Ankita Jha, Alain Garcia De Las Bayonas, Andrew J Saurin, and Thomas Lecuit. Modular activation of rho1 by gpcr signalling imparts polarized myosin ii activation during morphogenesis. *Nature Cell Biology*, 18(3):261–270, 2016.
- [77] David L Page, Andreas F Koschan, Sreenivas R Sukumar, Besma Roui-Abidi, and Mongi A Abidi. Shape analysis algorithm based on information theory. In *Proceedings 2003 International Conference on Image Processing*, volume 1, pages I–229. IEEE, 2003.
- [78] Andrew Wuensche. Basins of attraction in network dynamics. *Modularity in Development and Evolution*, pages 1–17, 2004.
- [79] Josephine T Daub and Roeland MH Merks. Cell-based computational modeling of vascular morphogenesis using tissue simulation toolkit. *Vascular Morphogenesis: Methods and Protocols*, pages 67–127, 2015.

## Contributions

D.K.D. conceived and designed the study, implemented the model, performed the analyses, and drafted the manuscript. N.T. contributed to the study design, provided feedback on the results and implications of the study, and commented on the manuscript at all stages. A.R.D.G. provided feedback on the results and implications of the study, and commented on the manuscript at all stages.

## Competing interests

The authors declare no competing interests.

## Materials & Correspondence

- All original code to generate the data in this study is publicly available, and can be found at <https://github.com/DominicDevlin/Stem-cell-differentiation-underpins-reproducible-morphogenesis>. Our code was adapted from the Tissue Simulation Toolkit [79].
- The genomes and associated data of all evolved organisms are also found in the above repository.
- Any additional information required to re-analyse the data reported in this paper is available from the lead contact upon request (ddev825@aucklanduni.ac.nz)

# Supplementary Information

Dominic K Devlin<sup>1\*</sup>, Austen RD Ganley<sup>1,2</sup>, and Nobuto Takeuchi<sup>1,3,4</sup>

<sup>1</sup>School of Biological Sciences, University of Auckland, Private Bag 92019,  
Auckland 1142, New Zealand

<sup>2</sup>Digital Life Institute, University of Auckland, Private Bag 92019,  
Auckland 1142, New Zealand

<sup>3</sup>Research Centre for Complex Systems Biology, Universal Biology Institute,  
University of Tokyo, Komaba 3-8-1, Meguro-ku, Tokyo 153-8902, Japan

<sup>4</sup>Department of Biology, Faculty of Sciences, Kyushu University, Fukuoka,  
Japan

\*ddev825@aucklanduni.ac.nz

March 26, 2025

**The Supplementary information includes:**

- Supplementary text S1 and S2
- Legends for videos S1 to S3
- Figures S1 to S9
- References for the supplementary text

**Other supplementary materials for this manuscript include the following:**

- Videos S1 to S3

## S1 Supplementary information on the trade-off between reproducibility and morphological complexity

This section aims to determine whether the difference in reproducibility scores between evolved organisms with and without stem-cell systems can be attributed to variations in their morphological complexity. To demonstrate the relationship between morphological complexity and reproducibility in our model, imagine the morphologically simplest organism: one that remains circular over development. The reproducibility of this organism will be trivially high because its circular morphology will not change in each developmental replicate. In contrast, morphogenesis requires extensive yet ordered cell movement. These extensive yet ordered movements are prone to noise in cell motion and geometry, which means that morphogenesis tends to become more susceptible to noise with increasing complexity of these cell movements. This relationship between complexity and reproducibility has also been demonstrated in a previous study [1].

To answer whether differences in reproducibility scores between evolved organisms with and without stem-cell systems can be attributed to variations in their morphological complexity, we first compared the average morphological complexity between the two groups using the technique outlined in Methods 5.5, averaged over 60 developmental replicates. We found that those with stem-cell systems ( $\mu = 94.1$ ,  $\sigma = 13.3$ ) exhibit lower morphological complexity on average than those without stem-cell systems ( $\mu = 116.5$ ,  $\sigma = 18.0$ ), and that this difference was statistically significant ( $p = 10^{-4}$ , two-tailed t-test). Although our quantification of morphological complexity is arbitrary, this result suggests that the difference in reproducibility scores may in part be explained by differences in morphological complexity.

We conducted two further analyses to more rigorously determine whether this difference in morphological complexity was responsible for the difference in reproducibility scores. For the first analysis, we examined whether “within-group similarity” differed significantly between organisms with and without stem-cell systems. Within-group similarity measures how similar the morphologies are within a group (with or without stem-cell systems). To quantify within-group similarity, we computed the morphological similarity of one developmental replicate of each organism within a group at 12,000 developmental time steps (DTS) to all others within the same group (determined by the maximum Jaccard index; see Methods 5.7). Suppose the morphologies within a group have low complexity. In this case, they will deviate little from the initial circular shape, resulting in higher morphological similarity and, thus, higher within-group similarity scores. Conversely, more complex morphologies will result in morphological dissimilarity and, thus, lower within-group similarity scores. The advantage of using within-group similarity to determine the link between reproducibility and complexity is that it can be compared to reproducibility scores, as it uses the same technique, while avoiding our arbitrary quantification of morphological complexity. The results show that organisms with stem-cell systems had a marginally higher within-group similarity (mean=45.5%) than organisms without (mean=43.9%,  $p = 0.036$  two-tailed t-test; Fig. S2D). Despite this marginally higher similarity, there was a significant overlap in the interquartile ranges between the two groups. Moreover, the difference in means of within-group similarity scores is much smaller than the difference in reproducibility scores, which were, on average, 72.1% for organisms with stem-cell systems versus 52.0% for organisms without ( $p < 10^{-12}$ , two-tailed t-test). This result indicates that the difference in morphological complexity between the groups does not fully account for their reproducibility differences.

For the second analysis, we conducted a regression to examine whether the relationship between morphological complexity and reproducibility differs between those with and

without stem-cell systems. The regression model we used is:

$$R_i = \beta_0 + \beta_1 \cdot M_i + \beta_2 \cdot (M_i \times \text{stem}_i) + \epsilon_i \quad (1)$$

where  $M_i$  and  $R_i$  are the morphological complexity and reproducibility of organism  $i$ , respectively. The term “stem <sub>$i$</sub> ” evaluates to one if organism  $i$  has a stem-cell system; otherwise, zero. We found that reproducibility declines more rapidly as complexity increases for those without stem-cell systems (95% confidence interval on  $\beta_1$  is  $[-3.0 \times 10^{-3}, -1.3 \times 10^{-3}]$ ,  $n = 65$ ), compared to those with them (95% confidence interval on  $\beta_1 + \beta_2$  is  $[-1.2 \times 10^{-3}, 1.9 \times 10^{-5}]$ ,  $n = 24$ ). Moreover, when organisms are matched for morphological complexity, the graph shows no obvious overlap between the two groups (Fig. S2D). This result indicates that the elevated reproducibility observed in organisms with stem-cell systems is not because of their lower morphological complexity than those without such systems.

The above result that reproducibility declines less with complexity in organisms with stem-cell systems suggests that organisms with stem-cell systems bypass a reproducibility-complexity trade-off. However, the sample sizes in the regression analysis are small as we only considered the 90 evolved organisms. Therefore, we increased our sample size by taking samples of many organisms from each simulation. We measured the reproducibility and average morphological complexity of the organism with the highest fitness in each population at 100-generation intervals throughout each simulation. We analysed 36 simulations: the 18 that evolved complex, highly reproducible morphologies via stem-cell systems and 18 that did not (we chose the latter based on having similar endpoint morphological complexity to the former), performing a linear regression of reproducibility against morphological complexity for each simulation separately. The results show that reproducibility declined with complexity in every simulation (Fig. S2F), indicating that organisms become less reproducible as they became more complex. However, the slopes appear steeper in simulations where poorly reproducible morphologies evolved (Fig. S2F). To quantify this, we bootstrapped the coefficients of the linear regression slopes to obtain a confidence interval of this coefficient for the 18 simulations where stem-cell systems did not evolve and the 18 where they did. We found that this coefficient was much higher in simulations where stem-cell systems did not evolve (95% CI of slope is  $-0.0035$  to  $-0.0029$ , Fig. S2FG, orange lines) compared to those where they did (95% CI of slope is  $-0.0017$  to  $-0.0011$ , Fig. S2FG, blue lines), indicating that reproducibility declines more rapidly as complexity increases. Moreover, the ability of morphological complexity to predict an organism’s reproducibility was better in simulations without stem-cell systems (average  $R^2 = 0.91$  across the 18 simulations) than in those with stem-cell systems (average  $R^2 = 0.59$  across the 18 simulations). These findings support the hypothesis that stem-cell systems allow organisms to bypass a trade-off between morphological complexity and reproducibility. Moreover, the fact that differences in reproducibility persist through evolution suggests that organisms with stem-cell systems are on different evolutionary trajectories than those without (these trajectories are likely determined by the initial conditions or early in the evolution of a simulation when stem-cell systems begin to evolve).

## Supplementary Videos

**Video S1: Organism-2 development for the 12,000 DTS.**

**Video S2: Organism-1 development for the 12,000 DTS.**

**Video S3: Organism-6 development for the 12,000 DTS.**

Supplementary Videos can be found at: <https://doi.org/10.6084/m9.figshare.28646858.v1>

## Supplementary Figures

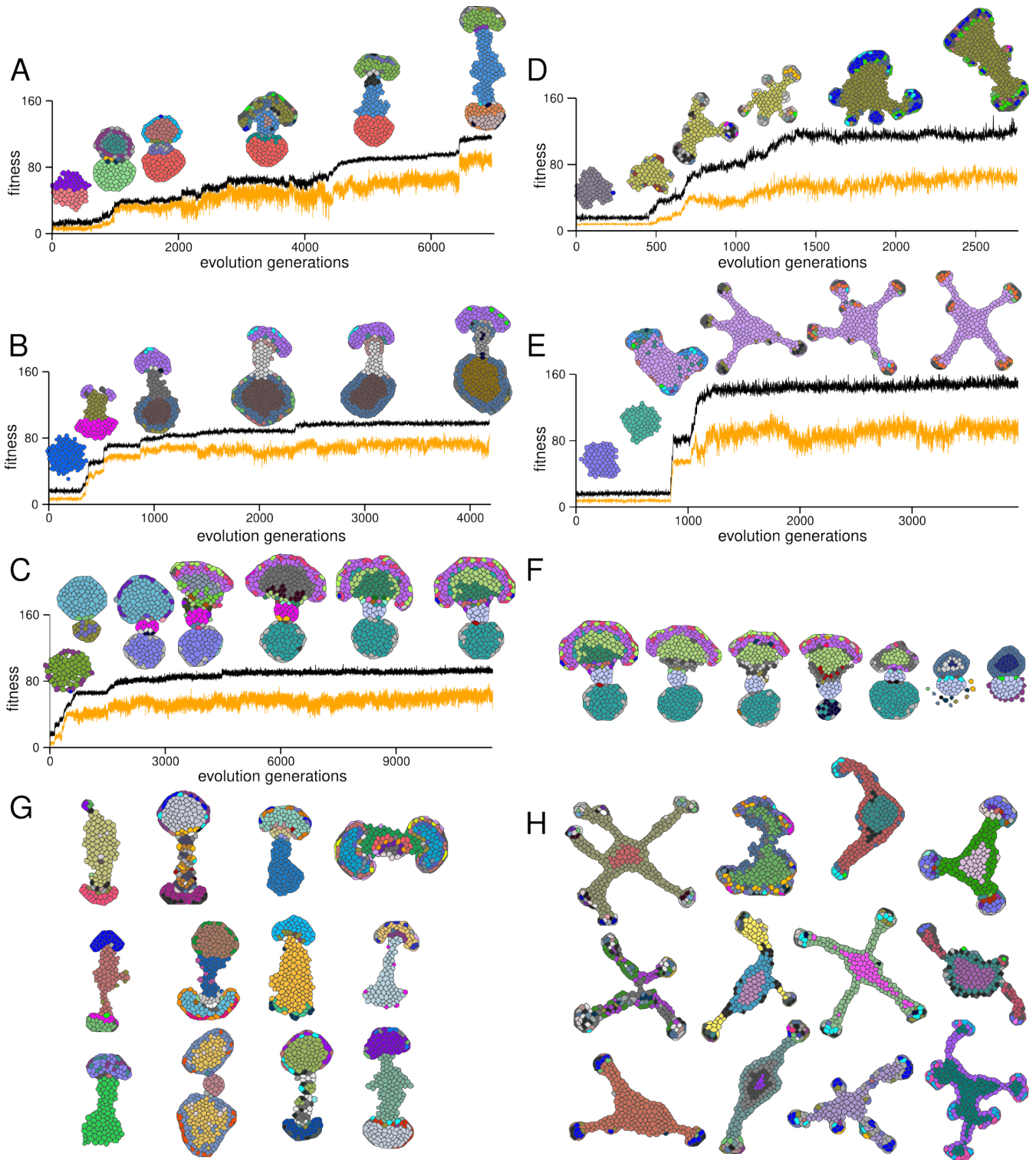


**Figure S1: Evolution and evolved organisms.** **ABC** Three plots of fitness evolution, each from a separate simulation where organisms with high reproducibility evolved. The black lines show the maximum recorded fitness at each generation. The orange lines show the average fitness of each generation. Above each plot are six or seven organism morphologies at the end of their development (12,000 DTS). Each morphology is taken from a separate generation and is the most morphologically complex in its generation, shown approximately above the generation it belongs to. **DE** Two plots of fitness evolution, each from a separate simulation where organisms with poor reproducibility evolved, mirroring the plots shown in (ABC). The evolutionary trajectories shown in (ABCDE) indicate that fitness reaches a plateau before  $2.5 \times 10^3$  generations in 5 out of 6 simulations (we ran all simulations for at least this number of generations). Plateaus appear to persist for a long time, as exemplified by (C), which we ran for 11,500 generations. We did not run simulations for  $>10,000$  generations due to computational limitations (10,000 generations takes approximately one week with 60 CPUs). The similarity of the organism morphologies above each plot indicates that a phenotypic “fixation” occurs through evolution. This fixation implies that the evolved organism accurately represents the evolutionary outcome of a simulation. **F** Morphological variation in a population due to mutation. Each morphology is an organism from the final generation from the simulation shown in (C). Each organism has a unique GRN topology due to mutations. **G** Zoo of highly reproducible and **H** poorly reproducible morphologies, each shown at the end of their development (12,000 DTS). Each morphology is a different evolved organism not shown in the main text.

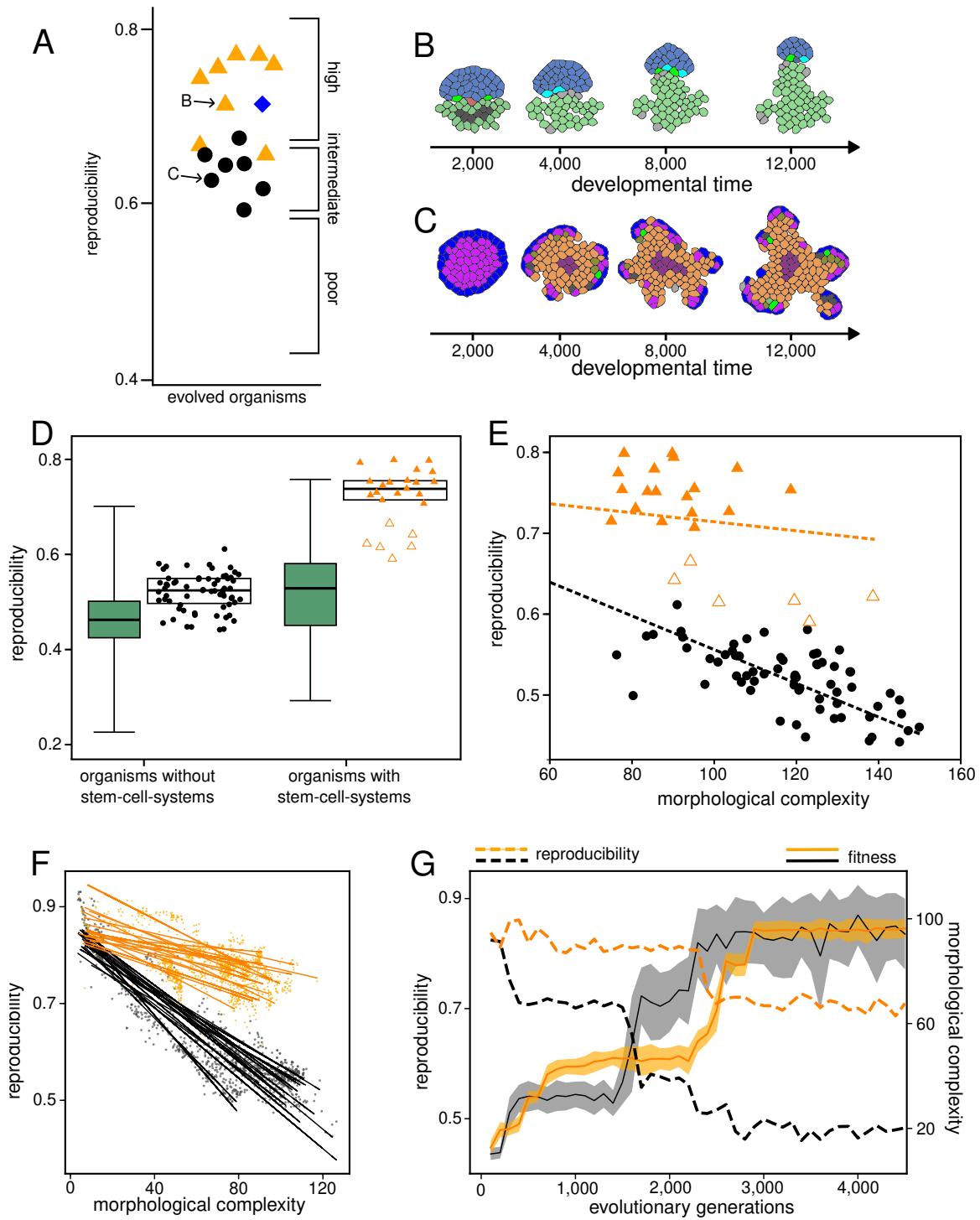




**Figure S2: The trade-off between morphological complexity and reproducibility.**

**A** Reproducibility scores of 16 of the 36 “failed evolved organisms” that did not reach the threshold for morphological complexity. We chose these 16 because their morphological complexity is above a score of 40 but below 70 (70 is the threshold we used to determine if an organism has a complex morphology in the original 126 simulations). The remaining 19 morphologies with scores below 40 were excluded because they have circular morphologies. Black circles are organisms that have state spaces with a single SCC, of which there are seven. The organism indicated by the blue diamond has a state space with multiple SCCs with no unidirectional transitions. It has a similar morphogenesis to the organism shown in Fig. S3D. Orange triangles are organisms with stem-cell systems, of which there are eight. Categories of “high”, “intermediate” and “poor” are copied from Fig. 3C in the main text. The arrows point to the organisms shown in (B) and (C). The eight organisms with stem-cell systems were significantly more reproducible than those without ( $p = 0.007$ , two-way t-test). **D** Within-group reproducibility scores of the 65 evolved organisms without stem-cell systems (left green box plot,  $n = 2211$ ) and the 24 with stem-cell systems (right green box plot,  $n = 276$ ). Boxes show medians and interquartile ranges (IQR). Whiskers show the range. Filled Orange triangles are reproducibility scores of organisms with stem-cell systems that are highly reproducible; unfilled orange triangles are organisms with stem-cell systems that are not highly reproducible. The black circles are organisms without stem-cell systems. The unfilled box plot shows the median and interquartile range of reproducibility scores for organisms with (right) and without (left) stem-cell systems. **E** Scatter plot of reproducibility scores against morphological complexity for the 90 evolved organisms. Data points are coloured and shaped as in (D). The black and orange dashed lines are the regression for poorly reproducible and highly reproducible morphologies described in Text S1. **F** Scatter plot of organism reproducibility scores against morphological complexity scores. Each data point is the most complex organism in a population from a generation, taken at intervals of 100 generations. The blue data points are organisms from simulations where highly reproducible organisms with stem-cell systems evolved (18 simulations, 1508 data points), whereas the orange data points are from simulations where poorly reproducible organisms without stem-cell systems evolved (18 simulations, 1180 data points). Each line is the linear regression performed on all data points from the same simulation, coloured in the same way as the data points. Performing a single linear regression across all blue data points gives a 95% confidence interval on the slope of  $-0.0011$  to  $-0.0099$  ( $R^2 = 0.32$ ). Performing a single linear regression across all orange data points gives a 95% CI on the slope of  $-0.0032$  to  $-0.0031$  ( $R^2 = 0.86$ ). **G** Evolution of reproducibility (dotted lines) and fitness (solid lines) in a simulation where a stem-cell system evolved (blue) and a simulation where one did not (orange). The data used to generate the lines is the morphological complexity and reproducibility of the highest-fitness organism in populations at intervals of 100 generations for each simulation. A stem-cell system is first observed in the simulation in orange at generation 500.

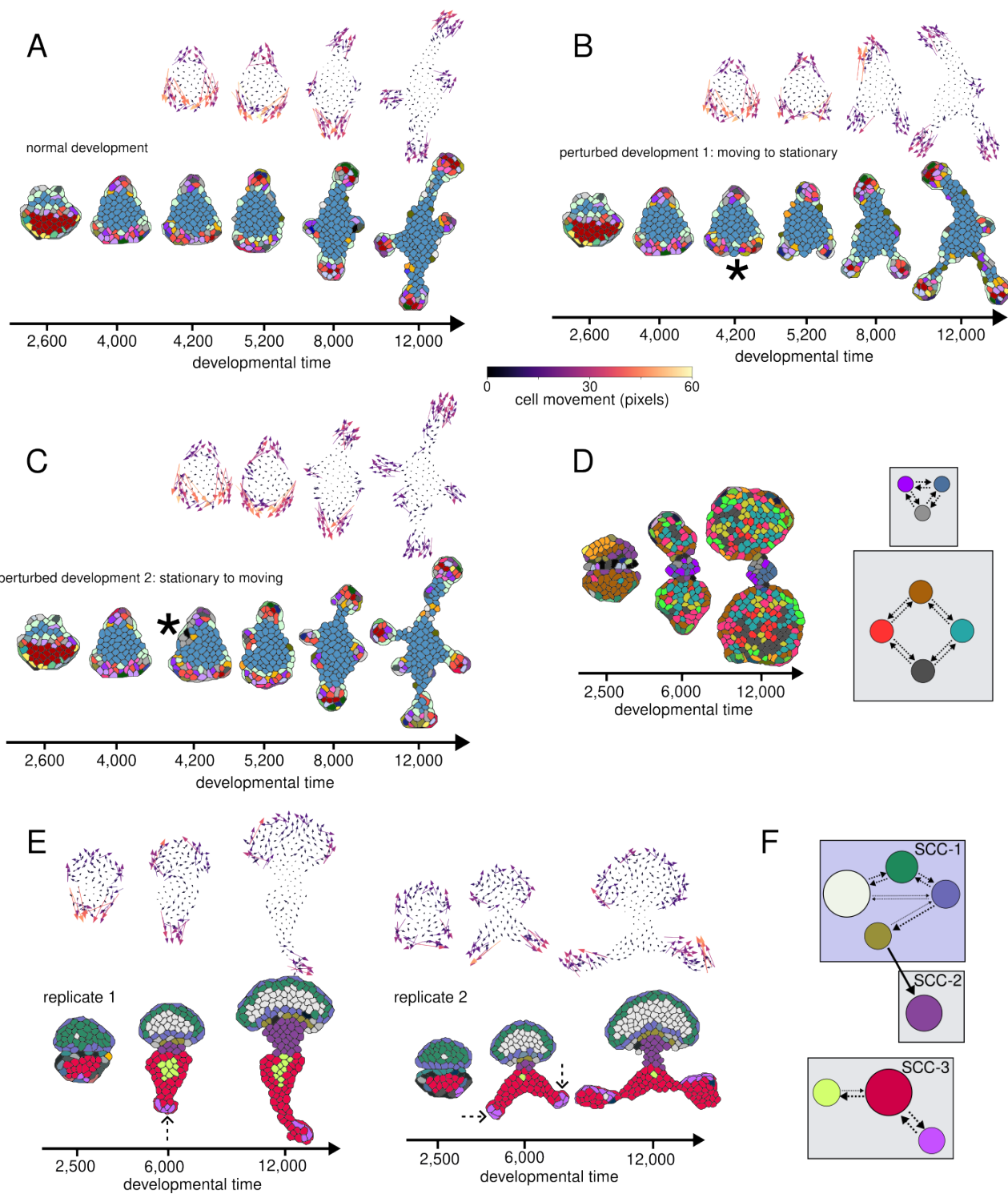
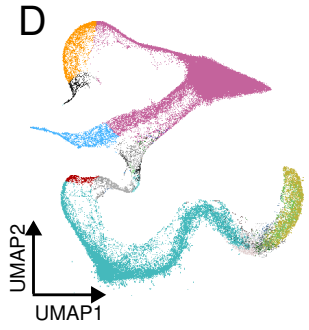
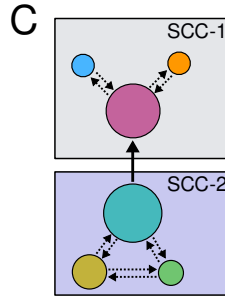
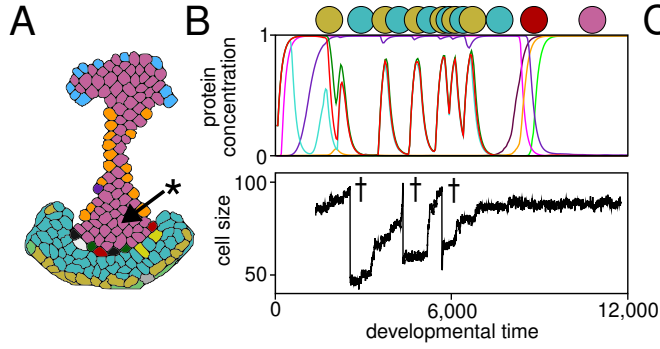
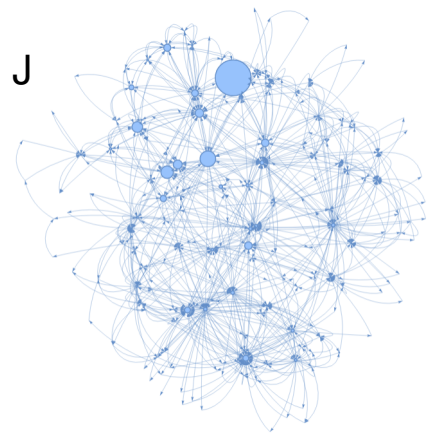
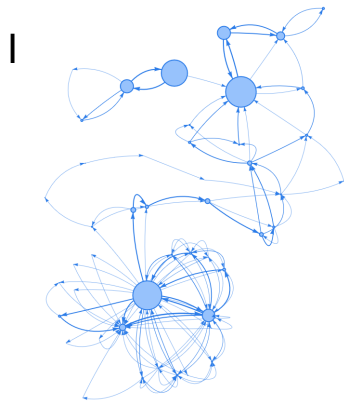
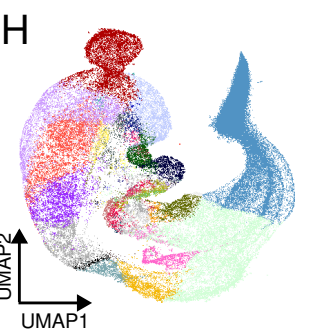
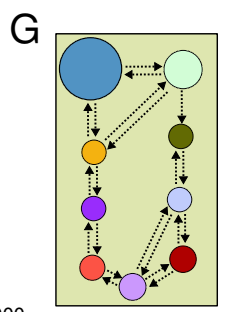
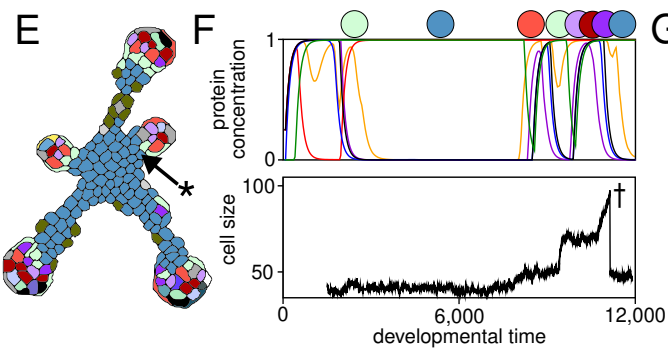


**Figure S3: The causes of poor morphogenetic reproducibility.** **A** Developmental replicate of organism-1 from the main text depicted at six DTS. Vector plots show the displacement of the centre of mass of each cell during 2,000 DTS at each respective time point, with colours indicating magnitude (the lighter, the larger). **B** A perturbed development of organism-1 using the same random seed as (A) to show that moving-to-stationary transitions cause bifurcations. Development was perturbed by artificially changing the protein expression profiles of three moving cells at the bottom of the organism to a stationary cell state (blue cells, indicated by the asterisk). We performed this perturbation after 4,100 DTS. This perturbation resulted in a bifurcation of collective cell motion, as indicated by the vector plots and the morphology. **C** A perturbed development of organism-1 using the same random seed as (A) to show that stationary-to-moving transitions cause protrusions. Development was perturbed by artificially changing the protein expression profiles of three stationary cells at the left flank of the organism to moving states (grey cells, indicated by the asterisk). We performed this perturbation after 4,100 DTS. This perturbation resulted in a protrusion, as indicated by the vector plots. **D** Development of the outlier organism categorised as having both a complex and reproducible morphology that does not have a stem-cell system (blue diamond in Fig. 3C), shown at three DTS during its development. Its state space shows cell states partitioned into two strongly connected components (SCCs, grey boxes) with no unidirectional transitions. The organism undergoes morphogenesis by stacking three circular balls of cells on top of each other. **E** Two developmental replicates of an intermediately reproducible morphology with vector plots showing the displacement of the centre of mass of each cell during 2,000 DTS at respective time points, with colours indicating magnitude (the lighter, the larger). Its state space, shown in (F), shows one stem-cell type (SCC-1), one differentiated-cell type (SCC-2) and one SCC (SCC-3) that is not part of the stem-cell system. The regions of the organisms corresponding to the stem and differentiated cell types appear morphologically similar between developmental replicates. In contrast, the region corresponding to cells in SCC-3, which is not part of the stem-cell system, appear dissimilar between developmental replicates. This dissimilarity arises because there is a bifurcation in the motion of these cells in replicate 2 but not in replicate 1 (dashed black arrows). This bifurcation occurs because both moving and stationary states are in SCC-3, as the vector plots confirm. Thus, this organism’s development shows properties of both highly (SCC-1 and SCC-2) and poorly (SCC-3) reproducible morphogenesis.

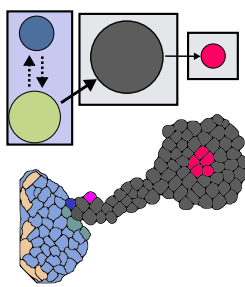
organism-1 (highly reproducible)



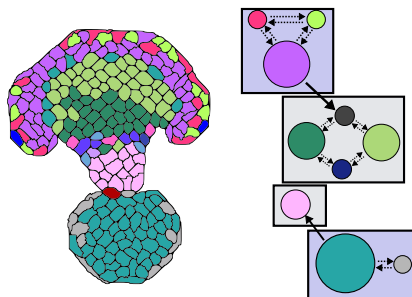
organism-2 (poorly reproducible)



**K** organism-3



organism-4



organism-5

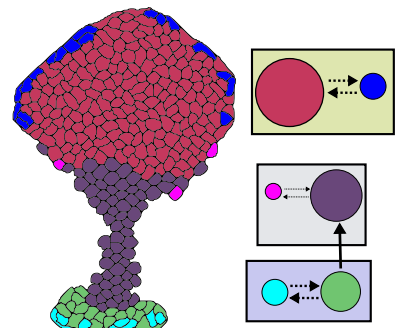


**Figure S4: Highly and poorly reproducible organisms have different cell-state transition dynamics.** Panels A through D correspond to organism-1 (highly reproducible), and panels E through H to organism-2 (poorly reproducible). **AE** Morphologies of organism-1 and organism-2 after the 12,000 DTS. **BF** Above the graphs are coloured circles depicting cell-state transitions for one cell, indicated by the asterisks in panels A and E, over the 12,000 DTS (some cell-state transitions are excluded for visibility). The top graphs show the concentrations of eight cell adhesion proteins over the 12,000 DTS. The bottom graphs show cell size over the 12,000 DTS. Daggers (†) indicate drops in size caused by cell division. **CG** Simplified cell state spaces consisting of cell states (nodes) and cell-state transitions (arrows). Node sizes depict cell state frequency. Cell states are partitioned into SCCs (coloured boxes). **DH** Visualisations of cell states (colours) mapped onto cell protein expression profiles (data points) that have undergone dimension reduction by UMAP. The data consists of 85,825 (D) and 115,625 (H) points, each collected from every cell at intervals of 40 DTS. **I** The state space shown in (C) without any pruning of cell states and cell state transitions. Many SCCs in the unpruned cell state space are “transitory”. These transitory SCCs consist of cell states observed during differentiation from SCC-1 to SCC-2. **J** The state space shown in (G) without pruning of cell states and cell state transitions. **K** Organisms 3, 4 and 5 from the main text are shown at the end of their respective developments (12,000 DTS), along with their simplified state spaces. The layout of the cell states in the morphology mirrors the layout of the cell states in the state space. The green box in the organism-5 state space corresponds to an SCC disconnected from the other two (i.e., no unidirectional transitions).

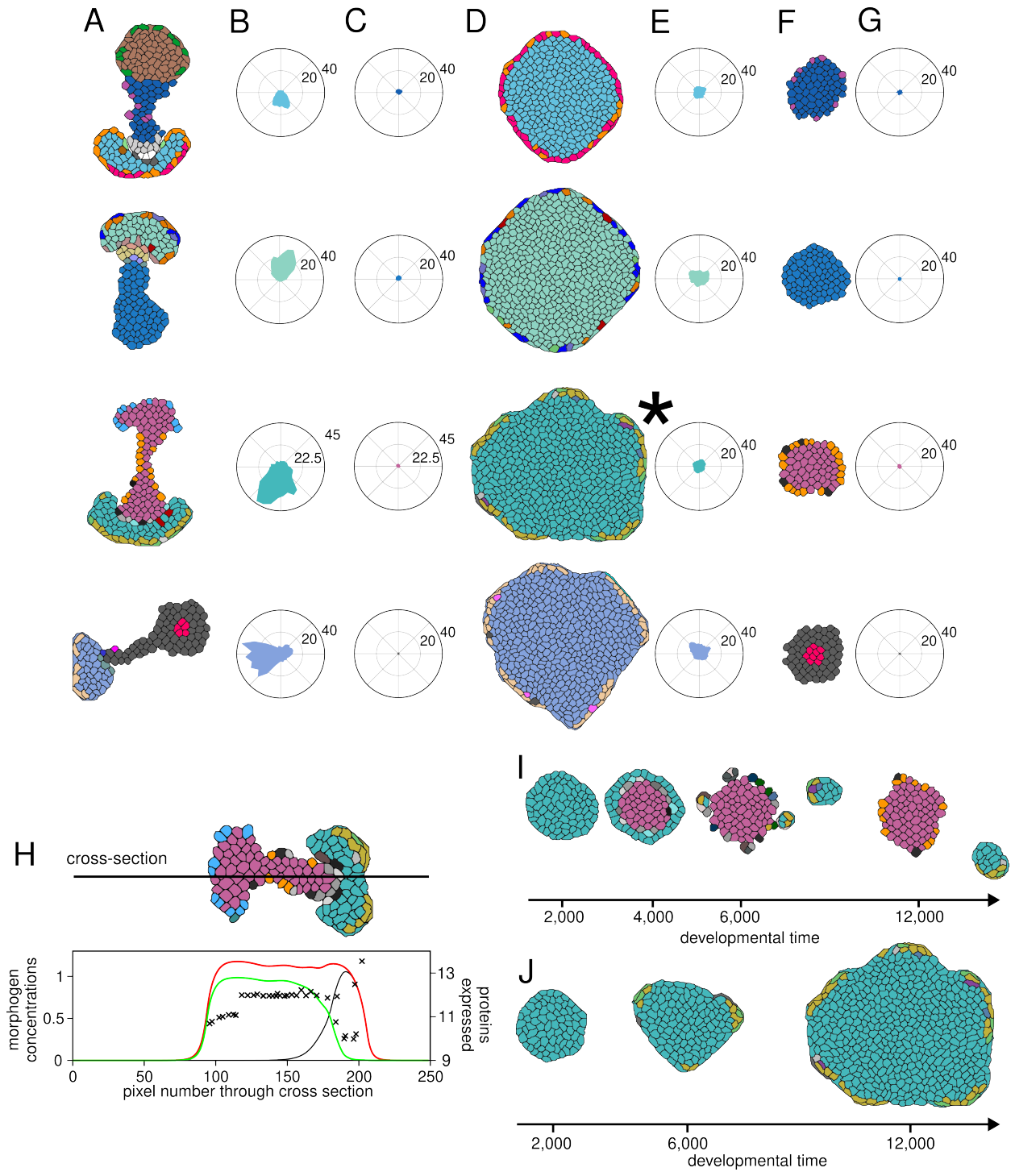


**Figure S5: Stem-cell motion is isotropic when isolated from other cell types.** **A** Four evolved organisms with stem-cell systems at their developmental endpoints (12,000 DTS). Each organism has one stem-cell type and one differentiated-cell type **BC** Polar plots of momentum magnitude by angle of momentum over normal development of the four organisms, separated by cell type; (B) shows plots for the four stem-cell types, where momentum appears anisotropic, and (C) shows plots for the four differentiated-cell types. **D** Isolated stem cells for each organism at their developmental endpoints (12,000 DTS). **E** Polar plots of momentum magnitude by the angle of momentum of the isolated stem cells for each organism, showing radially symmetrically distributed motion. **F** Isolated differentiated cells for each organism at their developmental endpoints (12,000 DTS). **G** Polar plots of momentum magnitude by angle of motion of the isolated differentiated cells for each organism. **HIJ** Analysis of stem-cell differentiation in organism-1. We show organism-1 here because its stem-cell type is one of the four (out of 30) that differentiates when isolated from other cell types. (H) shows morphogen concentrations along a cross-section of organism-1 at 8,000 DTS. The sum of cell protein concentrations is also shown for cells along this cross-section (each cross is one cell). The green morphogen induces stem-cell differentiation, which is produced by differentiated cells (data not shown). However, stem cells also begin to express the green morphogen themselves if the black and red morphogen concentrations get too high (data not shown). (I) shows the development of isolated type-1 stem cells after 2000, 4000, 6000 and 12,000 DTS. The isolated stem cells differentiate around the cluster's centre around 4,000 DTS. Differentiation begins at the cluster's centre because black and red morphogens are at their highest concentration, resulting in the expression of the green morphogen that induces differentiation. The differentiation of stem cells in this isolated organism causes stem and differentiated cells to split apart due to differential adhesion between stem and differentiated cells. **J** Development of organism-1 stem cells in isolation, except with morphogen concentrations prevented from increasing above 1.0. Preventing black and red morphogen concentrations from increasing above 1.0 stops the green morphogen from being expressed and thus prevents stem-cell differentiation. For the four stem-cell types that autonomously differentiate, including this one, we measured the motion anisotropy of isolated stem cells (plotted in Fig. 5F) after placing restrictions on morphogen concentrations to prevent differentiation. The asterisk in (DE) shows the morphology (D) and polar plot (E) of isolated stem-cell motion from organism-1 when these morphogen restrictions are in place.

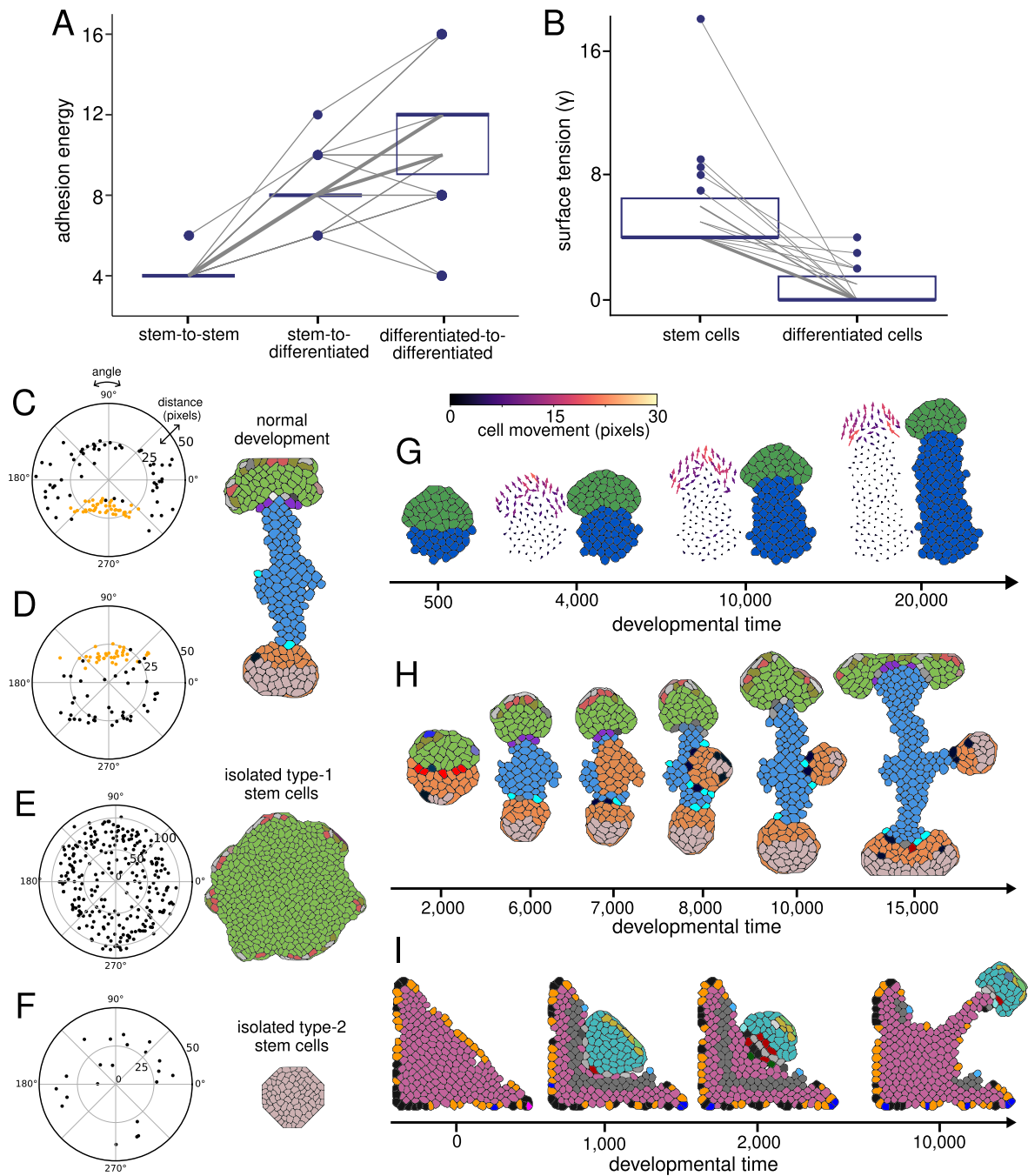




**Figure S6: Mechanisms of stem-cell system morphogenesis.** **A** Adhesion energy arising from stem-to-stem cell contacts, stem-to-differentiated cell contacts and differentiated-to-differentiated cell contacts across the 30 stem-cell systems from the 24 organisms with stem-cell systems. The grey lines connect adhesion energies from the same stem-cell system. Thicker grey lines indicate multiple stem-cell systems with the same data. Adhesion energies are the  $J_{ij}$  values arising from contact between the most frequently observed state of each cell type to itself (stem-to-stem or differentiated-to-differentiated) or the most frequently observed stem-cell state to its corresponding most frequently observed differentiated-cell state (stem-to-differentiated). Boxes show medians and interquartile ranges across the 30 stem-cell systems (The 25th and 75th percentiles are equal to the median for stem-to-stem and differentiated-to-differentiated adhesion energies; the 75th percentile is equal to the median for differentiated-to=differentiated adhesion energies). **B** The plot shows the surface tension ( $\gamma$ , explained shortly) for each stem-cell type ( $n = 30$ ) and each differentiated-cell type ( $n = 26$ ) across the 24 organisms with stem-cell systems. The median equals the 25th percentile (bottom of the box) because most stem-cell types have  $\gamma = 4$ , and most differentiated-cell types have  $\gamma = 0$ . The surface tension is  $\gamma = J_{ij} - J_{im}/2$ , where  $J_{ij}$  is the adhesion energy arising from contact between the most frequently observed state of each cell type to itself, and  $J_{im}$  is the adhesion energy arising from contact between the most frequently observed state of each cell type to the medium. Clusters of cells with  $\gamma \gg 0$  will tend to form circular morphologies, clusters of cells will tend to maintain the same shape as  $\gamma \rightarrow 0$ , and cells will disperse from each other when  $\gamma < 0$  [2]. **CDEF** Polar plots of stem-cell division distributions in space for both the normal development of organism-6 and isolated stem-cell development. (CD) show the spatial distribution of cell divisions (black) and differentiations (orange) for (C) type-1 and (D) type-2 stem-cell clusters, with the pole of the plots defined as the centre of mass of all of the respective stem cells in that cluster (i.e., the pole shifts as stem cells move over development). The location of a cell division is marked at the centre of mass of the parent cell. The plots show that type-1 stem cell divisions are asymmetric in that they occur around the cluster’s periphery rather than the centre. In contrast, type-2 stem cell divisions predominantly occur distal to the location of stem-cell differentiation. Asymmetric cell divisions in these two stem-cell clusters are caused by cycles of cell stretching and contraction due to oscillations in protein concentrations induced by morphogens at the cluster’s periphery (See Fig.S4BF for examples of protein concentration oscillations). (EF) show the spatial distribution of cell divisions for (E) isolated type-1 and (F) isolated type-2 stem-cell clusters. **G** A simplified model of organism-6 morphogenesis depicted after 500, 4,000, 10,000 and 20,000 DTS. We simplified organism-6 by allowing only two possible cell states, one with  $J_{ij} = 3$  (stem) and the other with  $J_{ij} = 12$  (differentiated).  $J_{im} = 6$  for all cells, and no contractile proteins exist. This model illustrates that elongation morphogenesis can occur through differential adhesion between only two cell states. Vector plots to the left of each morphology show the displacement of the centre of mass of each cell during 2,000 DTS at each respective time point, with colours indicating magnitude (the lighter, the greater). **HI** Customised stem-cell system morphologies. (H) shows the development of organism-6 from the main text, with development extended to 15,000 DTS. We customised its morphology by artificially changing the state of differentiated cells on the centre-right flank to type-2 stem cells, which causes a new branch to form. (I) shows the development of a triangular shape of stem and differentiated cells for 10,000 DTS. This simulation is analogous to Figure 5I of the main text, except using organism-1 stem and differentiated cells instead of those from organism-6.

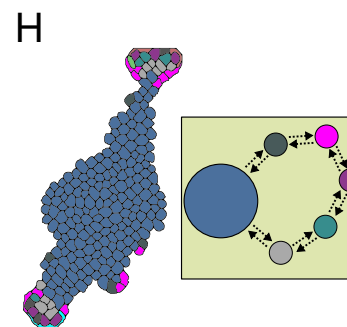
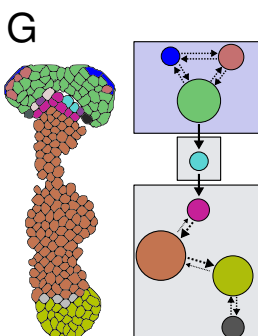
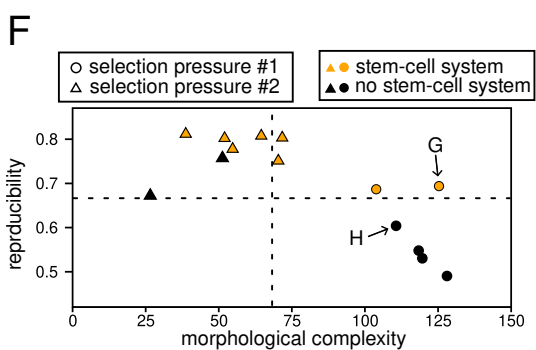
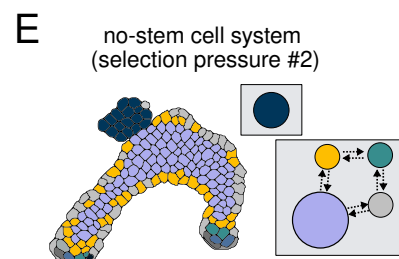
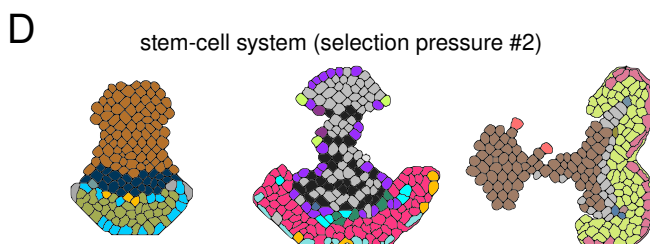
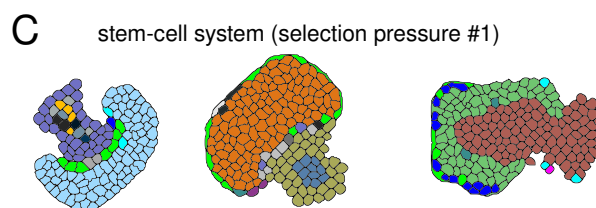
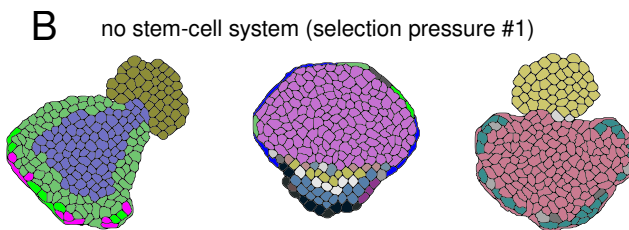
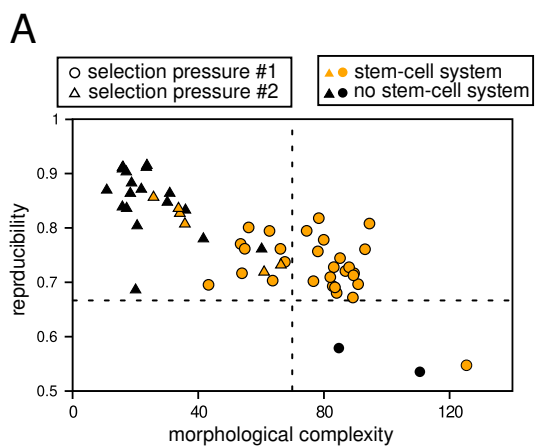


**Figure S7: Evolutionary accessibility of stem-cell systems.** **A** Reproducibility scores and morphological complexity of organisms evolved under two alternative fitness criteria. Fitness criterion #1 is how much an organism shifts its centre of mass over the 12,000 DTS (Methods 5.5). Fitness criterion #2 is a sum of the shift in the centre of mass criterion and the morphological complexity criterion (described in Section 2.6 and Methods 5.5 of the main text). Triangles are morphological complexity (not fitness) and reproducibility scores of evolved organisms from 25 simulations using fitness criterion #1. Circles are morphological complexity and reproducibility scores of the 31 evolved organisms from the simulations using fitness criterion #2. Data colour-coded orange indicates organisms with stem-cell systems. Data colour-coded black indicates organisms without stem-cell systems. The dashed line is a morphological complexity of 70, the threshold we used to determine if an organism was sufficiently morphologically complex in the original set of simulations, where the selection pressure was only morphological complexity (described in Methods 5.5). The dashed line at a reproducibility score of 66% is the cut-off for high reproducibility indicated in Figure 3C. **B** Three evolved organism morphologies after 12,000 DTS from simulations using fitness criterion #1 that did not evolve stem-cell systems. **C** Three evolved organism morphologies after 12,000 DTS from simulations using fitness criterion #1 that did evolve stem-cell systems. **D** Three evolved organism morphologies after 12,000 DTS from simulations using fitness criterion #2 that did evolve stem-cell systems. **E** Morphology, shown after 12,000 DTS, and state space of one of the two evolved organisms without a stem-cell system from the simulations using fitness criterion #2. Although the state space shows multiple SCCs, there is no unidirectional transition between them and thus no stem-cell system. **F** Reproducibility scores and morphological complexity of organisms evolved under alternative fitness criteria #1 and #2 using a minimal genome model. Colour coding, shape and dashed lines are the same as (A). The arrows point to the data points of organisms shown in (G) and (H). The minimal genome comprises 12 genes (as opposed to 26): six transcription factors (three of which are morphogens, two of which are maternal factors), four cell-cell adhesion proteins and two cell-medium proteins. The adhesion parameters that we changed to accommodate the new genome are  $J_{ij}^{max} = 20$ ,  $\phi_k^{ij} = 4$ ,  $J_{im}^{max} = 18$ ,  $\psi_1 = 10$  and  $\psi_2 = 2$ . There are no contractile proteins. **G** A highly reproducible evolved organism from the minimal genome model with a stem-cell system shown and its state space indicating multiple SCCs connected by a unidirectional transition. **H** A poorly reproducible evolved organism from the minimal genome model without a stem-cell system and its state space indicating a single SCC. Morphologies in (G) and (H) are shown after 12,000 DTS.

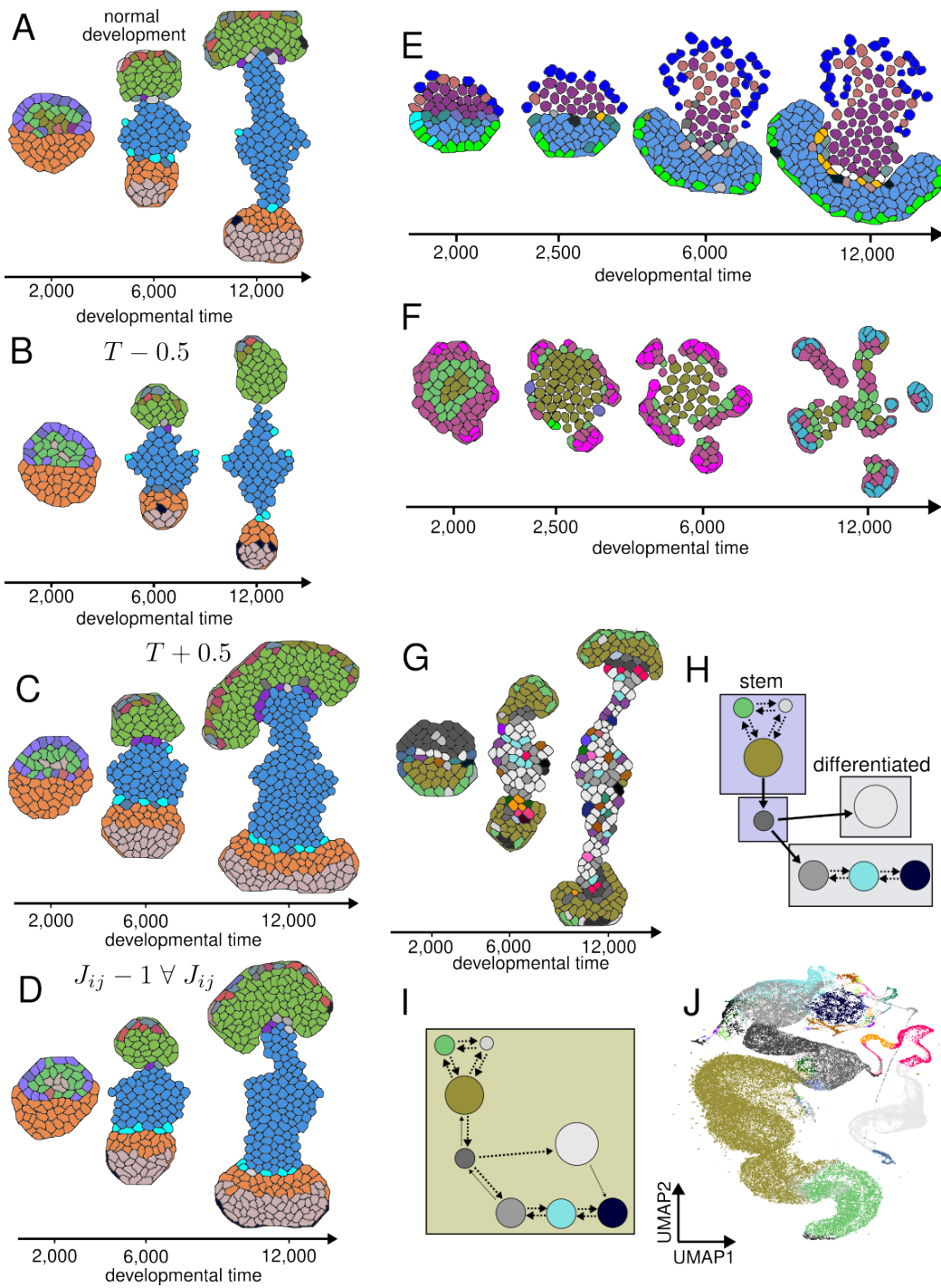


**Figure S8: Technical details of the model and analysis.** **ABCD** Robustness of organism-6 morphogenesis to changes in temperature and adhesion parameters. (A) shows the normal development of organism-6 after 2000, 6000 and 12,000 DTS. (B) shows the development of organism-6 using the same random seed as (A) but with the temperature,  $T$ , decreased by 0.5 (where  $T = 3$  by default). (C) shows the same development of organism-6 using the same random seed as (A) but with  $T$  increased by 0.5. (D) shows the same development of organism-6 using the same random seed as (A) but with all cell-cell adhesion energies,  $J_{ij}$ , decreased by one. **EF** Organisms that are designated 0 fitness because there is no single shape to measure the complexity of. We show the development of two organisms at four DTS. The cells of both organisms split up from each other during development. These organisms were arbitrarily chosen from evolving populations in evolutionary simulations. **GHIJ** One of the two organisms with stem-cell systems that has rare transitions from differentiated to stem cells (these rare transitions were removed during pruning). (G) shows a developmental replicate of the organism, and (H) shows its state space after pruning, indicating multiple SCCs with unidirectional transitions. (I) shows the same state space before the pruning of rare transitions (although rare cell states are pruned for clarity), indicating only a single SCC. (J) is a visualisation of cell states (colours) mapped onto cell protein expression profiles (points) that have undergone dimension reduction by UMAP for the organism shown in (G). Profiles are collected from four developmental replicates. Two lines in the UMAP plot connect the white cell state (deemed to be differentiated in the pruned state space) to other cell states. The thinner of the two lines corresponds to a transition of this differentiated cell state to the other differentiated cell state. This transition is one of those removed after pruning.

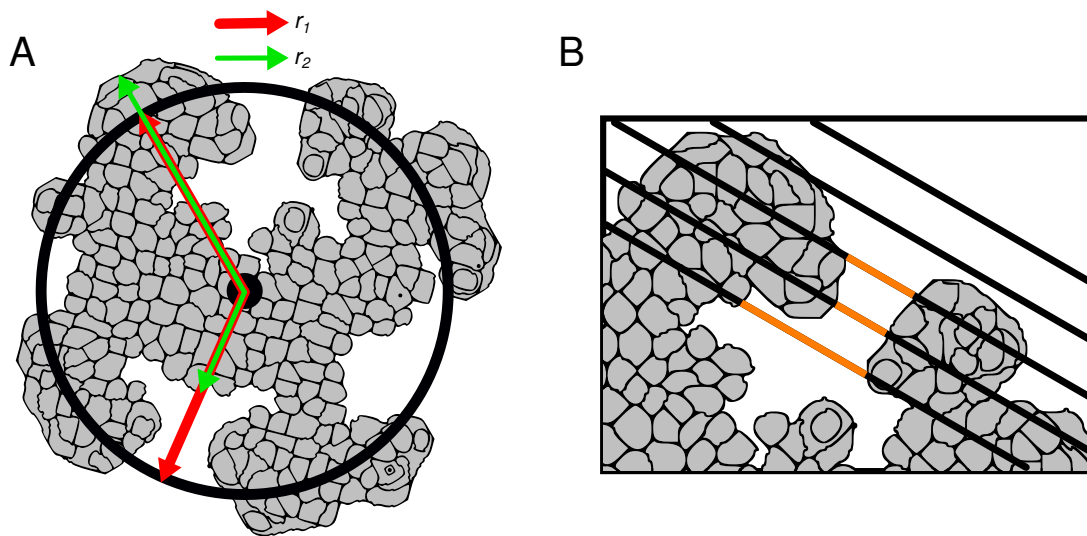


**Figure S9: Visual illustration of algorithm used to quantify morphological complexity.** **A** Visualization of the measure of deviation from a circle. We show the difference between the actual organism radius ( $r_1$ ) and the radius if all organism pixels were to be circularly distributed ( $r_2$ , black circle) at two locations. **B** Visualization of the measure of inward folds. Solid black lines depict the evenly spaced parallel lines drawn across the grid at one of the 12 evenly-spaced angles. The actual number of lines occur with a much higher frequency than the five shown here. The orange segments of the lines indicate “gaps” in the organism morphology. The square root of the total number of these gaps with a minimum length of 20 pixels is the organism’s negative curvature.

## References

- [1] Pascal F Hagolani, Roland Zimm, Miquel Marin-Riera, and Isaac Salazar-Ciudad. Cell signaling stabilizes morphogenesis against noise. *Development*, 146(20):dev179309, 2019.
- [2] François Graner and James Glazier. Simulation of biological cell sorting using a two-dimensional extended potts model. *Physical Review Letters*, 69(13):2013, 1992.